

A pragmatic strategy for implementing spatially correlated observation errors in an operational system: an application to Doppler radial winds

Article

Accepted Version

Simonin, D., Waller, J. A., Ballard, S. P., Dance, S. L. and Nichols, N. K. (2019) A pragmatic strategy for implementing spatially correlated observation errors in an operational system: an application to Doppler radial winds. *Quarterly Journal of the Royal Meteorological Society*, 145 (723). pp. 2772-2790. ISSN 1477-870X doi: <https://doi.org/10.1002/qj.3592> Available at <http://centaur.reading.ac.uk/84168/>

It is advisable to refer to the publisher's version if you intend to cite from the work. See [Guidance on citing](#).

To link to this article DOI: <http://dx.doi.org/10.1002/qj.3592>

Publisher: Royal Meteorological Society

All outputs in CentAUR are protected by Intellectual Property Rights law, including copyright law. Copyright and IPR is retained by the creators or other copyright holders. Terms and conditions for use of this material are defined in the [End User Agreement](#).

www.reading.ac.uk/centaur

CentAUR

Central Archive at the University of Reading

Reading's research outputs online



A pragmatic strategy for implementing spatially correlated observation errors in an operational system: an application to Doppler radial winds

D. Simonin^{a*}, J. A. Waller^b, S. P. Ballard^a, S. L. Dance^b, and N. K. Nichols^b

^a*MetOffice@Reading, Meteorology Building, University of Reading, Reading, Berkshire, RG6 6BB, United Kingdom*

^b*School of Mathematical, Physical and Computational Sciences, University of Reading, Reading, Berkshire, RG6 6BB, United Kingdom*

*Correspondence to: D. Simonin, MetOffice@Reading, Meteorology Building, University of Reading, Reading, Berkshire, RG6 6BB, United Kingdom. E-mail: david.simonin@metoffice.gov.uk

Recent research has shown that high resolution observations, such as Doppler radar radial winds, exhibit spatial correlations. High resolution observations are routinely assimilated into convection permitting numerical weather prediction models assuming their errors are uncorrelated. To avoid violating this assumption observation density is severely reduced. To improve the quantity of observations used and the impact that they have on the forecast requires the introduction of full, correlated, error statistics. Some operational centres have introduced satellite inter-channel observation error correlations and obtained improved analysis accuracy and forecast skill scores. Here we present a strategy for implementing spatially correlated observation errors in an operational system. We then provide the first demonstration of the practical feasibility of incorporating spatially correlated Doppler radial wind error statistics in the Met Office numerical weather prediction system.

Inclusion of correlated Doppler radial winds error statistics has little impact on the computation cost of the data assimilation system, even with a four-fold increase in the number of Doppler radial winds observations assimilated. Using the correlated observation error statistics with denser observations produces increments with shorter length scales than the control. Initial forecast trials show a neutral to positive impact on forecast skill overall, notably for quantitative precipitation forecasts. There is potential to improve forecast skill by optimising the use of Doppler radial winds and applying the technique to other observation types.

1. Introduction

Error characteristics of atmospheric observations are complex and not straightforward to derive. Each meteorological instrument is accurate to within a given tolerance subject to its engineering specifications. This is called instrument error. However, in the context of data assimilation, there is a representation error that arises in addition to the instrument error. The sources of representation error include the variability of the observed field at scales different from those resolved by the assimilating dynamical model, observation pre-processing and/or the approximation of the observation operator (Janjić *et al.* 2017). Therefore, the total observation error can be expressed as the sum of the instrument error and a representation error. It is generally assumed that instrument error is uncorrelated and unbiased (any existing biases are assumed to have been removed). In contrast the error of representation is generally correlated and state dependent (Waller *et al.* 2014).

Idealized studies have shown that incorporating correlated observation errors in data assimilation systems leads to a more accurate analysis (Stewart *et al.* 2013; Stewart 2010; Healy and White 2005) and to the inclusion of more observation information content (Stewart *et al.* 2008), particularly on small scales (Rainwater *et al.* 2015; Fowler *et al.* 2018). Studies with operational data have shown that satellite inter-channel errors can exhibit significant correlations (Stewart *et al.* 2009, 2014; Bormann and Bauer 2010; Bormann *et al.* 2010; Waller *et al.* 2016a), and accounting for them in the assimilation results in improvements in the forecast skill score (Weston *et al.* 2014; Bormann *et al.* 2016; Campbell *et al.* 2017), but may affect the number of iterations required to solve the variational minimization problem (Tabcart *et al.* 2018). More recent research has shown that observation errors can also be spatially correlated (Waller *et al.* 2016c,a; Cordoba *et al.* 2017).

The UK public weather service has an emphasis on accurate forecasts/nowcasts of strong convective storms which can be responsible for major flooding events. In response, the UK Met Office has an operational convection permitting numerical weather prediction (NWP) system using a 1.5km version of the Unified Model (UM) (Lean *et al.* 2008; Tang *et al.* 2013). Such

a system requires the assimilation of new, high temporal and spatial resolution observations in order to provide an initial state that contains information at suitable scales (Gao and Stensrud 2012; Sun *et al.* 2014; Clark *et al.* 2015; Ballard *et al.* 2016). Such observations include, for example, mode-S aircraft data (e.g. de Haan and Stoffelen 2012; Strajnar *et al.* 2015; Lange and Janjić 2016), weather radar (e.g. Caya *et al.* 2005; Wattrelot *et al.* 2014; Wang and Wang 2017) or high resolution AMVs (e.g. Velden *et al.* 2017). However, due to the presence of correlated errors, there has been no attempt to operationally assimilate observations at a high spatial density. Instead, the observations are assumed to be spatially uncorrelated; the data is thinned to separation lengths where this assumption is understood to be reasonable and the error variances inflated to account for any neglected correlations (Buehner 2010). As a result, the quantity of high resolution observations, such as those provided by weather radar in the form of reflectivity, radial wind (Simonin *et al.* 2014) and refractivity, is severely reduced. This may result in a sub-optimal analysis and poorer forecasts. Therefore, in order to assimilate observations at a high spatial density the observation error correlations must be considered.

This work proposes a pragmatic strategy that allows the use of horizontally correlated observation errors. We describe the implementation of such a strategy within the Met Office operational variational assimilation scheme. Practical feasibility and possible impacts are demonstrated with NWP trial experiments using spatially correlated observation error for Doppler radial wind.

First, we present the current assimilation system used at the Met Office in Section 2. Subsequently, in Section 3, we describe in detail the implementation of the proposed strategy that allows use of correlated observation error statistics. After presenting the experimental details in section 4, section 5 shows the impact of the new scheme when it is applied to Doppler radial wind observations for the assimilation system, the analysis and the forecasts. Finally we conclude in Section 6.

2. The current Met Office approach

In this section we describe the current Met Office variational data assimilation system software (VAR) and its parallelisation. We

79 also describe the current treatment of observation error statistics
80 in the assimilation.

81 2.1. The data assimilation system

82 In this section we describe some pertinent features of the current
83 Met Office variational data assimilation (VAR) software (Lorenc
84 *et al.* 2000; Rawlins *et al.* 2007). These schemes are based on the
85 incremental approach of Courtier *et al.* (1994) and are applicable
86 to 3D-Var and 4D-Var. Here we document them following the
87 notation of Ide *et al.* (1997).

88 Given a full resolution non-linear forecast model, incremental
89 variational assimilation seeks a simplified, perturbation model
90 state increment $\delta w^a \in \mathbb{R}^{n_s}$ to a full resolution guess field $\mathbf{x}^g \in$
91 \mathbb{R}^n such that the analysis at full resolution $\mathbf{x}^a \in \mathbb{R}^n$ at $t = T + 0$
92 is given by

$$\mathbf{x}^a = \mathbf{x}^g + \mathbf{S}^{-1} \delta \mathbf{w}^a. \quad (1)$$

93 Here, \mathbf{S}^{-1} is the incrementing operator; it is the generalised non-
94 linear inverse of a simplification operator \mathbf{S} which reduces the
95 full model's complexity and resolution to that of the perturbation
96 (Ide *et al.* 1997). In the Met Office VAR schemes, where the full
97 resolution non-linear model is the UM, the operator \mathbf{S} is also
98 used to simplify multiple moisture and cloud variables to a single
99 variable (Rawlins *et al.* 2007). We find the perturbation model
100 state, $\delta \mathbf{w}^a$, at $t = T + 0$ by minimizing a penalty function,

$$\begin{aligned} J(\delta \mathbf{w}) &= \frac{1}{2} (\delta \mathbf{w} - \delta \mathbf{w}^b)^T \mathbf{B}^{-1} (\delta \mathbf{w} - \delta \mathbf{w}^b) \\ &\quad + \frac{1}{2} (\mathbf{y} - \mathbf{y}^o)^T \mathbf{R}^{-1} (\mathbf{y} - \mathbf{y}^o) \\ &= J_b + J_o, \end{aligned} \quad (2)$$

101 where $\delta \mathbf{w} = \mathbf{S}(\mathbf{x}) - \mathbf{S}(\mathbf{x}^g)$ and $\delta \mathbf{w}^b = \mathbf{S}(\mathbf{x}^b) - \mathbf{S}(\mathbf{x}^g)$, $\mathbf{x}^b \in \mathbb{R}^n$
102 is the background model state, $\mathbf{B} \in \mathbb{R}^{n \times n}$ is the background
103 error covariance matrix and $\mathbf{R} \in \mathbb{R}^{p \times p}$ is the observation error
104 covariance matrix. The penalty function minimizes the fit of the
105 model state to the background state, J_b , and observations, J_o .
106 Note that the variational problem is solved iteratively using a
107 conjugate gradient method.

108
109 This work was conducted using a 3D-Var assimilation system
110 with a centered window using first guess at appropriate time

(FGAT: Fisher and Andersson 2001; Lorenc and Rawlins 2005). 111

The observations $\mathbf{y}^o \in \mathbb{R}^p$ are distributed within an assimilation 112
time window $[T - t_w, T + t_w]$. The background model state is 113
provided by a previous forecast and is interpolated in time to 114
the observation time. Following Lorenc and Jardak (2018), the 115
model prediction of the observations is given by $\mathbf{y} = H(\mathbf{G}\mathbf{x}^g +$ 116
 $\mathbf{G}\mathbf{S}^{-1}\delta \mathbf{w})$ where \mathbf{G} is the linear time- and space-interpolation of 117
the model generated field to the observation location and time and 118
 H is the non-linear observation operator. 119

In order to calculate the model prediction of the observations it 120
is necessary to interpolate the primary variables of the forecast 121
model and the perturbation forecast model to the observation 122
locations. Therefore, for each observation we define: 123

- The array $C_x = \mathbf{G}\mathbf{x}^g$ consisting of a vertical column of 124
the primary variables of the forecast model, interpolated 125
horizontally to the observation positions, valid at the 126
observation time. 127
- The array $C_w = \tilde{\mathbf{G}}\mathbf{S}^{-1}\delta \mathbf{w}$ consisting of a column of 128
the primary variables of the perturbation forecast model, 129
interpolated horizontally (and in time for 4D-VAR) to 130
the observation positions. 3D-Var treats all increments at 131
the same analysis time (in the middle of the window) 132
so $\tilde{\mathbf{G}}$ incorporates a space-interpolation only; FGAT is 133
implemented by the time-interpolation to the exact time of 134
each observation, in \mathbf{G} . 135
- The array \hat{C}_w , the derivative of the observation penalty 136
function (J_o) with respect to the primary variables of the 137
perturbation forecast model (C_w). 138

109 2.2. Parallelisation 139

The current approach to the parallelisation of the VAR code 140
follows the Data Parallel paradigm (Pacheco 1997, section 2.2.3): 141
all the processing elements (PEs) carry out the same operations 142
on different portions of the data set (figure 1 top panel). The data 143
is split into a number of geographical regions; this is known as 144
Domain Decomposition. 145

For VAR, the domain decomposition splits the C_w columns 146
such that each PE has information containing all the vertical 147
levels but only for a specified area of the horizontal-plane. The 148

149 PE IDs assigned to each column of C_w are stored in the vector
 150 $Cw_{PE} \in \mathbb{R}^p$.

151 As the observations are assumed to be independent and
 152 uncorrelated, they are simply spread across processors following
 153 the same regional decomposition as the model information (shown
 154 in figure 1). In this approach, the costs of the observation
 155 calculations are small compared to other components because
 156 there are no inherent message-passing or synchronisation delays.
 157 This advantage outweighs the inefficient load-balancing, for the
 158 domains typically used. The allocated PE ID for each observation
 159 is stored in the vector $Obs_{PE} \in \mathbb{R}^p$. This strategy is applied
 160 to all observation types and to the model information such that
 161 $Obs_{PE} = Cw_{PE}$.

162 2.3. Treatment of observation error statistics

163 Observation errors are typically assumed to be temporally
 164 uncorrelated, and with no correlations between observation types,
 165 so that \mathbf{R} is block-diagonal. This allows J_o to be calculated
 166 independently for each observation type and hence reduces the
 167 cost of the matrix-vector products in equation (2). Also, for
 168 many observation types, it is assumed that the observation errors
 169 are independent, Gaussian white noise, so that the associated
 170 observation error covariance sub-matrix for a given observation
 171 in equation (2) is diagonal (no cross-correlation) and contains
 172 the sum of instrument and representation errors $\mathbf{R} = \mathbf{E} + \mathbf{F}$
 173 (Lorenç et al. 2000). In this case the matrix-vector product
 174 simplifies to a series of scalar multiplications. There is one
 175 exception to this description. The current system accounts for
 176 correlated satellite inter-channel errors (Weston 2011; Weston
 177 et al. 2014). In this case, sets of observations with inter-channel
 178 error correlations provide information related to a single model
 179 column; hence the inclusion of correlated inter-channel error
 180 matrices is compatible with the current parallelisation strategy
 181 where observation and vertical model columns are distributed
 182 together between supercomputer processors (see Section 2.2 for
 183 a more detailed description). However, in the case of horizontally
 184 correlated observation error statistics, the existing data-structures
 185 do not allow the computation of the required matrix-vector
 186 products without excessive communication between processors.

187 3. The new approach

188 In this section we describe how the current Met Office variational
 189 data assimilation system software (VAR) has been adapted to
 190 exploit, and allow for, horizontal correlated observation error
 191 statistics.

192 3.1. Parallelisation

193 As shown in section 2.2, the assimilation system is using the same
 194 domain decomposition for observations as model. However, in
 195 order to make use of a full observation error covariance matrix,
 196 \mathbf{R}_s , (i.e. variance and correlation), it is necessary to gather error-
 197 correlated observations, and their model equivalent, on a single
 198 processor as shown in the bottom panel of figure 1.

199 To accommodate full observation error covariance matrices,
 200 the parallelization has been modified for observations that have
 201 mutually correlated errors. These observations are assigned to a
 202 *family* and sent to a single PE (figure 1 bottom panel) and are no
 203 longer distributed on a PE according to its geographical location
 204 but according to its family instead: $Obs_{PE} \neq Cw_{PE}$. If no family
 205 has been defined (observations with uncorrelated errors shown
 206 as blue dots in the bottom panel of 1), then the distribution of
 207 the information across the numerous processors is done in the
 208 traditional way (i.e domain decomposition $Obs_{PE} = Cw_{PE}$).

209 If some observations are believed to be correlated and
 210 associated to families, the main steps of the algorithm are:

- 211 • Each family of observations is assigned to a unique
 212 processor, following the Obs_{PE} assignment.
- 213 • The C_w 's are still distributed using the domain decomposi-
 214 tion (following the Cw_{PE} assignment), to allow horizontal
 215 interpolation to be a local operation on each PE.
- 216 • At each iteration, all the C_w 's associated with a family of
 217 observations are gathered into the processor assigned to this
 218 family.
- 219 • The observation penalty (J_o) is calculated.
- 220 • The last step is to redistribute the \hat{C}_w 's to their original
 221 location according to the Cw_{PE} assignment.

222 This new approach could significantly increase the communi-
 223 cation between processors. However, the added communications
 224 are not all-to-all; a set of lookup tables have been implemented

225 to ensure a "link" between Obs_{PE} and C_{wPE} . This restricts
 226 the communication to a minimum. In addition, the dissociation
 227 between the Obs_{PE} and C_{wPE} offers the opportunity to improve
 228 the load balancing. Observations are rarely uniformly distributed
 229 across the model domain, which implies that some processors will
 230 have more work than others if a domain decomposition is used.
 231 With this new approach, families can be allocated to the least
 232 loaded processor and improve the overall load balancing of the
 233 system. The only real limitation of this approach is in the defini-
 234 tion of families. For observation types such as radar observations,
 235 or GPS, where natural groupings exist, it is relatively easy to use.
 236 However for observations such as geostationary satellite imagery,
 237 where the entire model domain is covered by one single image, the
 238 creation of families is more difficult. One approach for this case
 239 is for families to represent a section of the domain, with extra
 240 observations forming a halo.

241 3.2. Treatment of observation error statistics

242 The proposed approach for using spatially correlated errors is to
 243 treat each family in a similar way to the current approach for
 244 inter-channel correlations mentioned in section 2: Since \mathbf{R} and its
 245 inverse change each assimilation due to the quality control process
 246 and observation availability, a Cholesky decomposition method
 247 is used to calculate the observation penalty, J_o as described in
 248 [Weston et al. \(2014\)](#). This avoids the need to compute the
 249 inverse observation error covariance matrix directly. The method
 250 requires positive definite symmetric matrices, which covariance
 251 and correlation matrices are by definition, and is computationally
 252 cheaper than alternatives such as Gaussian elimination. This
 253 approach for handling correlated observation errors relies on the
 254 full \mathbf{R} being block diagonal, otherwise it may be necessary to use
 255 an approximation method such as [Yaremchuk et al. \(2018\)](#).

256 For each family it is necessary to determine the full
 257 spatial observation error correlation matrix \mathbf{C} and a matrix of
 258 standard deviations \mathbf{D} . For families containing fixed observations
 259 (observations at the same locations at each assimilation step)
 260 it may be possible to store a single fixed observation error
 261 covariance matrix. However, as mentioned earlier, due to
 262 quality control procedures and the intermittent nature of most
 263 observations, the observation error covariance matrix for each

family will change at each assimilation step. It therefore makes
 sense to derive \mathbf{C} dynamically by simply providing a correlation
 function and a pre-derived correlation length scale for each type
 of family. For example \mathbf{C} may be derived using,

$$267 \mathbf{C}_{i,j} = e^{\left(\frac{-|\Delta y_{i,j}|}{L_r}\right)}. \quad (3)$$

where for a given family, $\Delta y_{i,j}$ is the separation distance between
 a pair of observations \mathbf{y}_i and \mathbf{y}_j and L_r is the correlation
 lengthscale. Similarly \mathbf{D} is constructed using pre-derived variance
 for each family.

After determining the full spatial observation error correlation
 matrix and matrix of standard deviations, the observation error
 covariance matrix $\mathbf{R}_f = \mathbf{DCD}$ and the observation penalty (J_o)
 can be calculated as follows:

1. Calculate a vector of observation minus model equivalent
 differences $d_o^b = (\mathbf{y}^o - \mathcal{H}(\mathbf{x}))$.
2. Calculate the sensitivity $\mathbf{q} = \mathbf{R}_f^{-1} (\mathbf{y}^o - \mathcal{H}(\mathbf{x}))$ using a
 Cholesky decomposition ([Golub and Van Loan 1996](#)).
 The Cholesky decomposition avoids the need to invert
 the observation error matrix. Instead the sensitivity is
 calculated by first factorizing $\mathbf{R}_f = \mathbf{UU}^T$, where \mathbf{U} is an
 upper triangular matrix, then solving for \mathbf{q} using forward,
 and backward substitution.
3. The total observation penalty J_o for the family is calculated
 by multiplying the sensitivity by the observation minus
 model equivalent differences,

$$287 J_o = \frac{1}{2} (\mathbf{y} - \mathcal{H}(\mathbf{x}))^T \mathbf{R}_f^{-1} (\mathbf{y} - \mathcal{H}(\mathbf{x})). \quad (4)$$

The gradient of J_o needed for the variational minimisation
 is calculated using,

$$\frac{\partial J_o}{\partial \mathbf{x}} = \mathbf{H}^T \mathbf{R}_f^{-1} (\mathbf{y}^o - \mathcal{H}(\mathbf{x})). \quad (5)$$

290 4. Experimental details

The model used in this study is the operational UKV model. It is
 a variable-resolution version of the nonhydrostatic UM ([Davies
 et al. 2005](#)), allowing an explicit representation of convective

294 processes as described in [Lean et al. \(2008\)](#). The horizontal
 295 grid has a 1.5-km fixed resolution on the interior surrounded
 296 by a variable-resolution grid that increases smoothly in size to
 297 4 km and has 70 vertical levels. The variable-resolution grid
 298 allows the downscaled boundary conditions, taken from the global
 299 model, to spin up before reaching the fixed interior grid. The
 300 initial conditions are provided from the operational 3 hourly 3D
 301 variational assimilation scheme that uses an incremental approach
 302 ([Courtier et al. 1994](#)) and is a limited-area version of the Met
 303 Office variational data assimilation scheme ([Lorenc et al. 2000](#);
 304 [Rawlins et al. 2007](#)). The assimilation uses a vertical adaptive
 305 mesh that allows the accurate representation of boundary layer
 306 structures ([Piccolo and Cullen 2011, 2012](#)).

307 The background error covariance has been derived using the
 308 Covariances and VAR Transforms software ([Wlasak and Cullen
 309 2014](#)), which is Met Office covariance calibration and diagnostic
 310 tool that analyses training data representing forecast errors
 311 using the National Meteorological Center (NMC) lagged forecast
 312 technique or ensemble perturbations. Here an NMC method
 313 has been applied to $(T + 6h) - (T + 3h)$ forecast differences to
 314 diagnose variances and correlation length scales.

315 For this study, we are using a 3DVar analysis system with
 316 first guess at appropriate time (FGAT). The background field
 317 is provided by a $T + 3$ forecast (actually time interpolated
 318 to observation time using fields every 30 minutes in the $3h$
 319 observation window for FGAT). In addition to Doppler radial
 320 winds used at the centre of the assimilation window, the analysis
 321 uses hourly surface synoptic observations of temperature, wind,
 322 pressure, humidity and visibility, hourly wind profiler data, hourly
 323 satellite radiances, satellite winds and aircraft data, radiosonde
 324 and hourly GPS water vapour paths (note that hourly refers to
 325 the frequency usage of the observation). Radar-derived surface
 326 precipitation rates available every 15 min are included via latent
 327 heat nudging from $T-0.5$ h to $T+0.5$ h and hourly cloud-cover-
 328 derived 3D relative humidity profiles via moisture nudging ([Jones
 329 and Macpherson 1997](#); [Dixon et al. 2009](#)). The nudging was
 330 done over a period surrounding the analysis time, in addition to
 331 incremental analysis updating of the 3D-Var analysis increments.

332 The Doppler radial winds are provided by 18 Doppler Weather
 333 radars spread over the United Kingdom. Each radar produces 5

plan position indicator (PPI) scans every 10 minutes. The Doppler
 radial winds are assimilated using a simple observation operator
 where the horizontal model background winds are projected onto
 the slant of the radar beam (vertical motion is ignored) ([Simonin
 et al. 2014](#)). To reduce the density of the observations, multiple
 observations are made into a single super-observation (3° by $3km$)
 and then thinned using Poisson disk sampling, as described in
[Simonin et al. \(2014\)](#).

The observation error correlation matrices are calculated
 dynamically as described in section 3. In the correlation matrices
 we only consider horizontal correlations; we neglect vertical
 correlations as there are unlikely to be multiple observations,
 and hence vertically correlated errors, in a single model column.
 Instead we assume that observation errors are correlated only if
 the observations are within a height band as described in [Waller
 et al. \(2016c\)](#). This assumption results in a sparse block diagonal
 observation error correlation matrix. Using this approach the
 number of observations in a family cannot exceed 2000. When
 Doppler radial wind observation errors are assumed uncorrelated,
 the standard deviations for the control experiment are based on
 those described in [Simonin et al. \(2014\)](#) and evolve with range,
 whereas when correlation is accounted for, the standard deviations
 and length scales L_r are based on those calculated in [Waller et al.
 \(2016c\)](#). A comparison of the variances from both observation
 error matrices (\mathbf{R}) is shown in figure 2 as a function of height
 for the 1° , 2° and 4° radar beams. The length scales L_r have been
 determined by fitting Markov functions (eq. 3) to the estimated
 horizontal correlations. We note that the length scales L_r are
 dependent on both the height of the observation and the radar
 beam elevation. Neither the prescribed variances nor length scales
 differ between radars. However, due to the intermittent nature
 of the observations, the observation error covariance matrices do
 differ between radars; similarly, for any given radar the error
 covariance matrices differ at each assimilation time.

The impact of including horizontally correlated Doppler radial
 wind errors was investigated by running three experiments using
 data for the period 1-20 May 2016. As shown in table 1, the
 Control experiment uses a diagonal observation error matrix,
 whereas both experiments Corr-R-3km and Corr-R-6km use a

373 correlated observation error matrix. The Control run and the Corr-
 374 R-6km experiment use a $6km$ thinning distance whereas the Corr-
 375 R-3km experiment uses a $3km$ thinning distance. We note that the
 376 Control run and the Corr-R-6km experiment use the same set of
 377 observations; therefore, comparisons between these experiments
 378 allow us to determine the impact of including spatially correlated
 379 observation errors in the system. Comparisons between the Corr-
 380 R-6km and Corr-R-3km experiments allow us to assess the impact
 381 of including denser observations (permitted by the inclusion of the
 382 correlated errors). Results from an additional experiment using
 383 the control's set-up with $3km$ thinning instead of $6km$ will be
 384 presented periodically to add context. This experiment (Diag-R-
 385 $3km$) is known to be sub-optimal with the analysis degraded
 386 compared to the control. Comparison to the other experiments
 387 will positively bias the impact of correlated observation error;
 388 therefore, the authors limit the discussion of this experiment in
 389 the manuscript.

390 5. Initial Results

391 The initial impact of including the correlated observation error
 392 when assimilating Doppler radial wind has been assessed in three
 393 ways. First, we consider the computational performance of the
 394 system and its operational viability. Then we consider the relative
 395 impact on analysis and innovation accuracy by considering
 396 observation-minus-analysis and observation-minus-background
 397 statistics. Finally general forecast performance and specific
 398 quantitative precipitation forecast verification are presented.

399 5.1. Variational data assimilation system performance

400 This section focuses on the performance of the variational data
 401 assimilation system (VAR) during the trial.

402 Both the Control and Corr-R-6km experiments used a thinning
 403 distance of $6km$, which yield an average of 2000 Doppler
 404 radial wind observations per cycle. The Corr-R-3km experiment,
 405 however, use a reduced thinning distance of $3km$, which
 406 provides on average four times more (8000) Doppler radial wind
 407 observations per assimilation cycle.

408 Table 2 shows the average iteration and evaluation count for
 409 each experiment. The iteration and evaluation count from each
 410 run are very similar. (Note that one evaluation is one calculation

411 of the penalty function, and one iteration is equivalent to one cycle
 412 of the minimisation algorithm). This result is most significant
 413 when considering that the Corr-R-3km experiment used four
 414 times more Doppler radial wind observations. When comparing
 415 the mean iteration/evaluation count to the standard deviation we
 416 find that for all experiments there are substantial differences
 417 observed between different assimilations. The large variance is
 418 expected since we are using a regional data assimilation system
 419 where the total number of observations can change significantly
 420 depending on the time of assimilation (e.g. day vs. night). We note
 421 that when comparing timeseries of iteration/evaluation counts
 422 there are minimal differences between the three experiments (not
 423 shown) and all follow a diurnal cycle.

424 Table 2 also shows the average and standard deviation of
 425 the of observation and background penalty values (J_o and J_b
 426 respectively). The changes in the mean value of J_o and J_b
 427 suggest that the overall observation weight is reduced and more
 428 importance is given to the background information as shown from
 429 theoretical studies by Seaman (1977) or Stewart *et al.* (2008).
 430 This is evident when Corr-R-6km is compared to the Control as
 431 both experiments use the same observation count. Corr-R-6km
 432 has an increased (reduced) observation (background) penalty. As
 433 values of J_o and J_b are affected by the observation count, Corr-R-
 434 $3km$ needs to be compared to a Control experiment using $3km$
 435 thinning (Diag-R- $3km$). The comparison of Corr-R- $3km$ with
 436 Diag-R- $3km$ gives similar results to the Corr-R-6km/Control
 437 comparison. The mean values of J_o and J_b for Diag-R- $3km$ are
 438 equal to 9679.28 and 2277.59 respectively, whereas for Corr-R-
 439 $3km$ these values are equal to 10134.63 and 2050.53. The decrease
 440 in background penalty between Diag-R- $3km$ and Corr-R- $3km$
 441 more or less matches the increase in observation penalty between
 442 the two experiments.

443 Table 3 shows the performance of the assimilation over
 444 the trial period, as well as over 10 iterations, for the three
 445 experiments. Comparing the experiments we see that the increased
 446 communication did not impact on the performance of the code.
 447 The cost of computing J_o is minimal compared to that of J as
 448 wells as the wall-clock time. The cost of J_o remains minimal and
 449 there is little change in the total cost of J even when correlated
 450 observation error are used and observation count is increased.

Overall results show that the proposed strategy to introduce correlated observation error statistics does not diminish the computational performance of the assimilation system. Furthermore, denser observations with correlated errors can be assimilated without increasing the computational cost.

5.2. Impact on the analysis

Residual ($O - A$) and innovation ($O - B$) statistics provide a quantitative measurement of the impact of the correlated observation error upon the analysis for individual observation types. The $O - A$ are retrieved from the assimilation system as the residual at the end of the minimisation. First, we note that the mean bias from the innovation or the residual for this Doppler radial wind will always tend toward zero for a large quantity of observations due to the radial nature of the observation (Salonen et al. 2007). Instead figure 3 shows the $O - B$ and $O - A$ standard deviation (σ_{O-B} and σ_{O-A} hereafter) from the Control, Corr-R-6km and Corr-R-3km as a timeseries for each cycle over the of the trial. The time series of Doppler radial wind's σ_{O-B} , yield similar results, with mean σ_{O-B} over the length of the trial for the Control, Corr-R-6km and Corr-R-3km is equal to 2.77, 2.76 and 2.73 respectively. Here the background is a $T + 3$ forecast from the previous cycle (3 hourly data assimilation system). More pronounced differences between the control and the experiments are visible in the Doppler radial wind's σ_{O-A} (figure 3). In the case of Corr-R-6km (figure 3-a), the values of σ_{O-A} are consistently slightly higher than those for the Control. In the case of Corr-R-3km (figure 3-b) the σ_{O-A} are comparable to the values yielded by the Control.

The differences in σ_{O-A} between the two runs with identical observation count (i.e. Control and Corr-R-6km) confirm the results of the previous section. Despite the fact that the observation error matrix used in Corr-R-6km had smaller or equivalent variance compared to those prescribed for the Control experiment (figure 2), the weight of the Doppler radial wind observations was reduced in Corr-R-6km. This in turn reduces the fit to the observations and increases analysis error. This increase in analysis error is not seen in the Corr-R-3km's experiment where the σ_{O-A} shows similar values compared to the Control. The reduction in the observation weighting has been reversed by the increased

observation count. This is supported by considering the additional Diag-R-3km experiment, where σ_{O-A} is consistently lower (mean value of 1.20) compared to the Control (mean value of 1.57).

Before considering the impact on other observation types, we first consider how the structured wind increments may have been modified by the introduction of correlated observation error. Figure 4 shows the mean length scale, the mean variance and maximum values of the zonal wind increment at each model level over the trial. Length scale is simply defined as the fourth root of the ratio of the variance of a field (ϕ) and the variance of its Laplacian (calculated using a second-order finite difference approximation) (Descombes et al. 2015); that is

$$\mathbf{L} = \left(\frac{8 \cdot \text{variance}(\phi)}{\text{variance}(\nabla^2 \phi)} \right)^{1/4}. \quad (6)$$

We note that the mean increment can be related to systematic error in either observations or the model (Rodwell and Palmer 2007). However it has been shown that the Doppler radial wind observations used here are unbiased (Simonin et al. 2014). When the correlated observation error covariance matrix is introduced (Corr-R-6km) the zonal wind increment becomes smoother with smaller extremes at all model levels. The introduction of correlation acts as a low-pass filter, reducing the weight from individual observations and increasing the importance of the background information. This is consistent with the results from the σ_{O-A} . However, increasing the observation density (Corr-R-3km) counterbalances the effect of the correlated \mathbf{R} , by increasing the amplitude and the variance of the increment values at all levels so that the values are closer to the Control experiment. It produces increments with smaller length scales than the Control from the assimilation of denser observations which are more able to represent smaller scale features.

We now consider the impact from the introduction of the correlated observation error covariance matrix for the Doppler radial wind on the fit to other observations assimilated during the trial. Figure 5 shows the trial average ratio of σ_{O-A} and σ_{O-B} , between the experiments and the Control for all the wind observation types used in the trial. The error bars shown in figure 5 and subsequent figures, represent the 95% confidence

level. Due to high statistical variability between cycles, one should only consider the significant values to assess the impact. Most trial average innovation and residual standard deviations from the Corr-R-6km and Corr-R-3km yield smaller values compared to the Control, with Corr-R-3km outperforming Corr-R-6km. This trend is not completely homogeneous with, for example, mixed impact for the scatterometer wind (not statistically significant). Although not significant, the $O - A$ and $O - B$ from Corr-R-6km, exhibit a degradation for meridional wind from Sonde and Aircraft respectively. Note that Sonde U and V account for radiosonde profiles as well as wind-profiler observations. For all wind observations, the additional Diag-R-3km produces innovation and residual values (figure 5) that never improve upon the results of either the Corr-R-6km or Corr-R-3km. Furthermore, the innovation and residual values are significantly worse compared to the Control, with a decrease in analysis and background accuracy reaching 1% and more on a few occasions. For example, compared to the Control, U and V wind from Sonde are degraded by 2% in the σ_{O-A} and at least 0.5% in the σ_{O-B} . Note that Corr-R-3km shows an improvement of 0.5% in the σ_{O-A} and at least 0.75% in the σ_{O-B} .

The reduction in analysis error and improved innovations are equally visible when considering the results from satellite observations (figure 6). Again the general impact is stronger for Corr-R-3km. For the rest of the surface and upper-air observations (figure 7), the impact seen when considering Corr-R-6km is very much neutral, whereas Corr-R-3km still shows benefit. The statistics for relative humidity and potential temperature observations from sonde are neutral to negative in the σ_{O-A} (7-a), but improve in the σ_{O-B} (7-a). Again the additional Diag-R-3km (not shown) produces residual values that are worse compared to the Control with a maximum increase of 3% for relative humidity. Also, the σ_{O-B} do not outperform the Corr-R-6km or Corr-R-3km experiments. For satellite observations, Diag-R-3km has small overall improvement in comparison to the Control (0.3% in σ_{O-B}). However, Corr-R-6km or Corr-R-3km experiments are still significantly superior.

We now summarize the results from this section. From the analysis of $O - B$ and $O - A$ it is clear that the introduction of correlated observation error for the Doppler radial winds had a

general benefit in reducing the analysis error. From the results of the residual statistics (σ_{O-A}) and the shape of the wind increments, we see that the introduction of correlated observation error has a multi faceted effect (Daley 1991). The changes in the σ_{O-A} from Corr-R-6km experiment compared to the Control, as well as the observation and background penalty values, demonstrated that the Control experiment settings were producing an analysis that was over-fitting the Doppler radial wind. The use of a diagonal observation-error covariance matrix when observation errors are clearly horizontally correlated (Waller *et al.* 2016c) produced a suboptimal analysis (Liu and Rabier 2003). When the observation errors are correlated with a length scale of 20-30km (Waller *et al.* 2016c), thinning the data to a 6km spacing does not result in negligible error correlations between assimilated observations. By introducing correlated observation error statistics in the assimilation algorithm (Corr-R-6km), the assimilation algorithm acts like a low-pass filter on the observation increments. Reducing the thinning distance shows benefit only when the correlation in the observation errors are accounted for as demonstrated by results from Corr-R-3km. Omitting the correlation when using a dense network of observations, only produces a sub-optimal system, where dense observations are over-fitted and the general analysis error is increased. By contrast accounting for correlation when using a dense network of observations, increases the potential number of neighbour observations y_j to an observation y_i , allowing for synergy between more pairs of observations, as described by Fowler *et al.* (2018), as well as allowing the information content from smaller scales to be exploited. This transforms the assimilation algorithm and allows it to behave more like a high pass filter compared to the Corr-R-6km setting.

We support these results using simple model experiments (details are given in the appendix). We designed three experiments to imitate the changes in observation density between the Control, Corr-R-6km and Corr-R-3km experiments. Figure 8 shows the eigenvalues of the analysis error covariance matrix in observation space for the three simple model experiments:

- The Control experiment is qualitatively similar to the simple model experiment shown as a black curve in

figure 8. Here the simple model is using a diagonal observation error covariance but the true observation error covariance contains some correlation and the state is half observed.

- The Corr-R-6km experiment has a similar character to the simple model experiment shown as a gray curve in figure 8, where a correlated observation error covariance is used and the state is half observed.
- The Corr-R-3km experiment is qualitatively similar to the simple model experiment shown as a black dashed curve in figure 8. A correlated observation error covariance is used and the state is fully observed.

Figure 8 shows that assimilating observations with the correct error statistics reduces the analysis uncertainty at all scales compared to the case when the observation error correlations are neglected. However, in the case where the observation density is coarse, most of the reduction in analysis uncertainty is seen at large scale (grey curve of figure 8). Increasing the observation sampling when correlated observation errors are used, further reduces the analysis uncertainty. However, this time the additional reduction in uncertainty takes effect at small scales (dashed curve of figure 8), which is consistent with the analysis of our experiments.

5.3. Forecast performance

This section focuses on the impact on the forecast from the introduction of Doppler radial wind's correlated observation error.

5.3.1. Overall forecast performance

In order to quantify forecast skill of a variable such as temperature, wind or cloud cover it is possible to check the root mean square (RMS) or the equitable threat score (ETS) difference (Ebert *et al.* 2003) between an observed quantity and its forecast equivalent at a range of lead times, from T+6 to T+36 at 6-hour intervals. The forecast value at observation locations is calculated from a simple bilinear interpolation of the forecast taking a distance-weighted average of the four surrounding grid point values. From the values derived following the above process an index that summarizes this skill score can be determined so as to make it easier to tell how a given trial experiment is performing with respect to the Control.

The Met Office's UK NWP Index is defined as a weighted average of T+6 to T+36 skill scores over the UK domain, for 1.5m temperature, 10m wind (speed and direction), precipitation (equal to or greater than 0.5, 1.0 and 4.0 mm over the preceding 6 hours), total cloud amount (equal to or greater than 2.5, 4.5 and 6.5 oktas), cloud base height (given at least 2.5 oktas and equal to or less than 100, 500 and 1000 m above ground) and near-surface visibility (equal to or less than 200, 1000 and 4000 m).

Table 4 shows the results of the surface verification as percentage of improvements. For the Corr-R-6km UK NWP index changes by -0.005% compared to the Control run. For the Corr-R-3km UK NWP index changes by $+0.021\%$ compared to the Control run. Neither trial presents statistically significant differences in skill with respect to the Control run.

5.3.2. Impact on precipitation

So far we have concentrated our effort on the validation of the forecast performance overall. However, one of the main motivations of convective-scale assimilation is to improve short-term quantitative precipitation forecasts (QPF). Verification methods have conventionally been designed to assess the model forecast at point locations only. However, the temporal and spatial intermittent nature of a parameter such as rain makes these approaches unsuitable in general (Droegmeier 1997). This problem is amplified in this study because the 1.5 km model resolution is high enough to represent small-scale features and local variability. In response to this problem, a growing list of methods to verify precipitation forecasts based on the physical realism or spatial closeness to observations have been developed (Gilleland *et al.* 2009). Some techniques have concentrated on object verification (Ebert and MacBride 2000; Davis *et al.* 2006; Johnson and Wang 2013) by classifying rain features according to their characteristics. Other methods have focused on the spatial error and one such score is the Fractions Skill Score (FSS) introduced by Roberts and Lean (2008). The FSS provides a measure of the spatial agreement between two fields by comparing the fractional differences in the coverage of rain over differing sized squares (neighborhoods) centered at every grid square. More about the definition and use of the FSS can be found in the original paper by Roberts and Lean (2008) and then subsequently

683 in Roberts (2008), Mittermaier and Roberts (2010) or Skok
 684 (2015). Here the two fields of hourly accumulations of surface
 685 precipitation are from the forecast itself and the radar composite
 686 of derived rain rate.

687 Figure 9 shows the difference in fraction skill score between
 688 the experiments (Corr-R-6km: figure 9-a; Corr-R-3km: figure 9-
 689 b) and the Control as a Hinton diagram for different forecast lead
 690 times and different thresholds of hourly rainfall accumulation. The
 691 sign and the amplitude of the change in FSS values (ΔFSS) are
 692 shown with the color and size of the square respectively: positive
 693 values (positive impact) are shown as grey squares, whereas
 694 negative values (negative impact) are shown as black squares.
 695 The introduction of the correlated observation error only (Corr-
 696 R-6km) does not show any real impact on precipitation (figure
 697 9-a). The ΔFSS values are small ($\max|\Delta FSS| = 0.009$) with an
 698 almost homogeneous distribution of positive and negative impact.
 699 The results are more promising when the correlated observation
 700 error is introduced in association with an increase in observation
 701 density (figure 9-b). The ΔFSS values are larger compared to
 702 the previous comparison, but more importantly, a positive impact
 703 can be seen until $T + 7$ forecast lead time. The biggest positive
 704 impact is found for low threshold values (e.g. 0.2mmh^{-1} and
 705 90^{th} percentile).

706 Note that the FSS values for the Control forecasts, for a
 707 neighbourhood size of 41 grid boxes, were all well above 0.6
 708 indicating an already skillful forecast; although little impact can
 709 be seen over the entire period of the fully cycled trial, individual
 710 cycles do show some improvements. Figure 10 gives an example
 711 of the sort of differences that can be seen and shows an hourly
 712 accumulated precipitation $T + 3$ forecast valid at 1500 UTC on
 713 the 7th of April 2016, for Control, Corr-R-6km, and Corr-R-3km.
 714 During the 7th of April 2016, a band of showers developed and
 715 moved southwards, producing heavy precipitation on the east and
 716 central part of the UK. Compared to the observed radar derived
 717 hourly rain accumulation (figure 10-a), the Control (figure 10-b)
 718 produced showers that were typically too sparse and locally far too
 719 intense. The Corr-R-6km improved the shower coverage, but the
 720 real benefit of including correlated observation error is visible in
 721 the Corr-R-3km experiment (figure 10-d), where shower coverage

and intensity was noticeably improved. This is supported by the
 FSS value shown in figure 10-e and f.

The improvement seen in this particular forecast can be
 attributed to the change in observation weight. When accounting
 for correlated observation error the observation uncertainty
 information is no longer mutually independent. This results in a
 small down-weighting of the observations as demonstrated by the
 Corr-R-6km experiment (Figure 4). This effect results in a small
 benefit to the forecast and FSS (Figure 10c and e) as the Control
 experiment was over-fitting the Doppler radial wind producing
 broad analysis increments (Figure 4). Increasing the observation
 density in conjunction with correlated observation errors negates
 the smoothing effect seen in Corr-R-6km. The use of more
 accurate error statistics enables an improved representation of the
 small scale information content from the observation resulting in
 a more balanced analysis increment (Figures 4 and 8). Over time
 the small scale information propagates through the system and
 produces improved forecasts as seen in Figures 10d.

6. Conclusions

In this work, we provide a pragmatic strategy that allows
 the use of correlated observation errors in a high dimensional
 data assimilation system. We describe the implementation of
 this strategy in the Met Office system and then present a study
 demonstrating the practical feasibility of including horizontally
 correlated Doppler radial wind observation error statistics and
 its impact using an operational NWP system. The new strategy
 was achieved by altering the usual Data Parallel paradigm; rather
 than distributing observations with correlated errors using a
 domain decomposition, the observations are instead distributed
 in families that have mutually correlated errors as described in
 section 3.1. The second significant change relates to the actual
 use of the horizontally correlated observation errors statistics in
 the derivation of the observation penalty. This was implemented
 following the description presented in section 3.2.

A trial has been run for 20 days using the Met-Office UKV
 model configuration and 3D-Var, including a Control experiment
 with the operational settings (diagonal \mathbf{R}), an experiment using
 the operational settings with a correlated observation error

760 covariance matrix, and an experiment using correlated observation
761 error statistics with increased observation density.

762 Analysis of the impacts from the introduction of Doppler radar
763 radial wind horizontal correlated observation errors on the data
764 assimilation system and forecast skill have also been presented.
765 The introduction of correlated observation error has changed the
766 response from the variational system as follows:

- 767 • Introducing horizontal correlated observation errors
768 improves the $O - A$ and $O - B$ statistics in both
769 experiments. This suggests that the Control settings
770 with a diagonal observation error covariance matrix causes
771 the assimilation to over-fit Doppler radial observations.
- 772 • The positive impact of the introduction of correlated
773 observation error is stronger on the $O - A$ and $O - B$
774 statistics when dense observations are used. We showed
775 that introducing the correlated observation error, whilst
776 keeping the observation density fixed, has little impact
777 on the analysis uncertainty at the small scales. However
778 this is remedied by increasing the observation density
779 that introduces additional observation information at small
780 scales.
- 781 • The inclusion of correlated observation error statistics
782 allows dense observations to be assimilated without
783 detriment to the analysis quality.
- 784 • We showed that by accounting for the correlation in
785 the Doppler radial wind observation error, observation
786 density can be increased without any degradation to the
787 computational speed of the assimilation system.

788 Our results suggest that the use of a diagonal \mathbf{R} (Control
789 experiment) created a suboptimal system, where a $6km$
790 observation thinning distance was too dense (e.g. [Liu and Rabier](#)
791 [\(2003\)](#) or [Stewart et al. \(2008\)](#)). As shown for example by [Daley](#)
792 [\(1991\)](#) or [Fowler et al. \(2018\)](#) the system's responses to correlated
793 observation error are complex and make use of observation
794 information at specific scales. However, we showed that the
795 general behavior of the data assimilation system is comparable
796 to what can be expected using a simple model.

797 The impact on the forecast is more subtle. A small positive
798 signal can be seen when the observations are compared to the

model background within the assimilation system. This indicates
that the impact on the forecast lasts long enough to improve the
model background and consequently benefit the assimilation in
a cycling NWP system. Regarding the conventional verification
scores, the results indicate that over the length of the forecast there
is a small positive impact, if any. A stronger signal is visible in
the QPF scores. A positive impact can be seen until a forecast
lead time of $T + 7$. The biggest positive impact is found at low
threshold values, which implies an improvement in the location of
the rain. For all verification scores, the increase in the observation
density yields better results.

To the best of our knowledge this is the first operational
implementation of horizontal correlation observation errors in
a data assimilation system for numerical weather prediction.
Despite a marginal impact on the forecast, the introduction
of the correlated observation error allows the assimilation to
make better use of the observations by allowing the assimilation
of very dense observation networks, such as radar, without
any cost (no significant increase of wall clock time) to the
assimilation. We note that we have only considered the impact
for a single case study (20 days). Furthermore, the only alteration
in the experiments has been the inclusion of the correlated
observation errors. Further studies are required to analyse the
impact for different meteorological conditions. Improved settings
for operational parameters associated with Doppler radial wind
assimilation may also benefit the forecast. This may include
testing for statistical consistency of background and observation
errors using the diagnostic of ([Desroziers et al. 2005](#)). In addition,
since this work, the Met-Office operational system for convective
scale numerical weather prediction system has been upgraded to
4D-VAR. Therefore this system is now being extended to the 4D-
VAR framework.

Appendix

Here we present a simple example to help explain the results given
in Section 5.

In statistical linear estimation theory, the analysed state, x^a , is
given by

$$\mathbf{x}^a = \mathbf{x}^b + \delta \mathbf{x}^a = \mathbf{x}^b + \tilde{\mathbf{K}} \mathbf{d}_b^o, \quad (7)$$

836 where δx^a is the analysis increment, x^b is the background state,
837 \mathbf{d}_b^o the innovation vector,

$$\mathbf{d}_b^o = y^o - \mathbf{H}x_b, \quad (8)$$

838 and $\tilde{\mathbf{K}}$ the gain matrix,

$$\tilde{\mathbf{K}} = \tilde{\mathbf{B}}\mathbf{H}^T(\mathbf{H}\tilde{\mathbf{B}}\mathbf{H}^T + \tilde{\mathbf{R}})^{-1}. \quad (9)$$

839 The matrices $\tilde{\mathbf{B}}$ and $\tilde{\mathbf{R}}$ are the assumed background and
840 observation error covariance matrix respectively.

841 To understand the impact on the analysis of using a sub-optimal
842 observation error correlation matrix we consider the analysis
843 error covariance matrix, \mathbf{A} . If we know the exact background
844 error statistics, $\tilde{\mathbf{B}} = \mathbf{B}$, but are knowingly using an incorrect
845 observation error covariance matrix, $\tilde{\mathbf{R}} \neq \mathbf{R}$ then the analysis
846 error covariance matrix is given by,

$$\mathbf{A} = (\mathbf{I} - \tilde{\mathbf{K}}\mathbf{H})\mathbf{B} + \tilde{\mathbf{K}}(\mathbf{R} - \tilde{\mathbf{R}})\tilde{\mathbf{K}}^T. \quad (10)$$

847 We consider the impact on the analysis error covariance using
848 three simple model experiments. We assume that our background
849 is evaluated on 128 equally spaced points in a 1D periodic
850 domain, $(-32\pi, 32\pi]$. In order to compare with the results given
851 in Section 5 we consider two different observation operators, one
852 in which the full state is observed and one where the state at
853 every other grid point is observed. We further assume that the
854 true observation and background error statistics are homogeneous
855 and are defined, as in Waller *et al.* (2016b), using a second order
856 auto regressive function with length scales 5 and 10 respectively.
857 For our first experiment we assume that we observe half the state
858 and only know the observation error variance and hence neglect
859 the correlations i.e. $\tilde{\mathbf{R}} = \mathbf{I}$. For the second experiment we observe
860 half the state, but this time use the correct \mathbf{R} matrix. Finally we
861 increase the observation density and observe all grid points and
862 assume the correct \mathbf{R} matrix.

863 In all three experiments the matrices \mathbf{R} , $\tilde{\mathbf{R}}$ and $\mathbf{H}\mathbf{B}\mathbf{H}^T$ are
864 circulant matrices. Since the sums, products and inverses of
865 circulant matrices are circulant, $\mathbf{H}\mathbf{A}\mathbf{H}^T$ is also circulant. The
866 eigenvalues of circulant matrices are positive and can be found

using a discrete Fourier transform and consequently may be 867
ordered according to wave number. In this case the order of 868
the eigenvalues has a relation to the scales in the analysis error 869
in observation space. Therefore, the eigenvalues of the analysis 870
error covariance in observation space allows us to understand 871
the uncertainty we have at different scales in the analysis in 872
observation space. The k^{th} eigenvalue, ϕ_k , of a circulant matrix 873
 $\mathbf{C} \in \mathbb{R}^{N \times N}$ associated with frequency $\omega_k = \frac{2\pi k}{\Delta_x N}$, and sampling 874
interval Δ_x , is, 875

$$\phi_k = \sum_{n=0}^{N-1} c_n e^{-\frac{2\pi k n i}{N}}, \quad (11)$$

where c_n is the n^{th} coefficient of the first row of the circulant 876
matrix. In our experiments, due to the different number of 877
observations, the size of $\mathbf{H}\mathbf{A}\mathbf{H}^T$ changes. However, by analysing 878
the results as a function of wavenumber we can compare 879
physically consistent quantities. The results for our experiments 880
are plotted in Figure 8 and discussed in Section 5. 881

Acknowledgement 882

Susan P. Ballard passed away after a long illness on 12 July 2018, 883
during the manuscript drafting process. 884

J. A. Waller, S. L. Dance and N. K. Nichols were funded in part by 885
the NERC grants NE/K008900/1 Forecasting Rainfall exploiting 886
new data Assimilation techniques and Novel observations of 887
Convection (FRANC) and Towards END-to-End flood forecasting 888
and a tool for Real-time catchment susceptibility (TENDERLY) 889
and in part by the NERC National Centre for Earth Observation. 890

The authors would also like to thank Alison Fowler, Ross 891
Bannister, Andrew Lorenc and Stephen Oxley for their valuable 892
discussions. 893

The data used in this study may be obtained on request, subject to 894
licensing conditions, by contacting the corresponding author. 895

References 896

Ballard SP, Li Z, Simonin D, Caron JF. 2016. Performance of 897
4D-Var NWP-based nowcasting of precipitation at the Met 898
Office for summer 2012. *Quarterly Journal of the Royal* 899
Meteorological Society **142**(694): 472–487, doi:10.1002/qj. 900
2665. 901

- 902 Bormann N, Bauer P. 2010. Estimates of spatial and interchannel
903 observation-error characteristics for current sounder radiances
904 for numerical weather prediction. I: Methods and application
905 to ATOVS data. *Quarterly Journal of the Royal Meteorological
906 Society* **136**(649): 1036–1050, doi:10.1002/qj.616.
- 907 Bormann N, Bonavita M, Dragani R, Eresmaa R, Matricardi
908 M, McNally A. 2016. Enhancing the impact of IASI
909 observations through an updated observation-error covariance
910 matrix. *Quarterly Journal of the Royal Meteorological Society*
911 **142**(697): 1767–1780, doi:10.1002/qj.2774.
- 912 Bormann N, Collard A, Bauer P. 2010. Estimates of spatial
913 and interchannel observation-error characteristics for current
914 sounder radiances for numerical weather prediction. II:
915 Application to AIRS and IASI data. *Quarterly Journal of
916 the Royal Meteorological Society* **136**(649): 1051–1063, doi:
917 10.1002/qj.615.
- 918 Buehner M. 2010. Error statistics in data assimilation: Estimation
919 and modelling. In: *Data Assimilation Making Sense of
920 Observations*, Lahoz W, Khattatov B, Mènard R (eds), ch. 4,
921 Springer, p. 99.
- 922 Campbell WF, Satterfield EA, Ruston B, Baker NL. 2017.
923 Accounting for correlated observation error in a dual-
924 formulation 4d variational data assimilation system.
925 *Monthly Weather Review* **145**(3): 1019–1032, doi:
926 10.1175/MWR-D-16-0240.1.
- 927 Caya A, Sun J, Snyder C. 2005. A comparison between the
928 4dvar and the ensemble kalman filter techniques for radar data
929 assimilation. *Monthly Weather Review* **133**(11): 3081–3094,
930 doi:10.1175/MWR3021.1.
- 931 Clark P, Roberts N, Lean H, Ballard S, Charlton-Perez C.
932 2015. Convection-permitting models: A step-change in rainfall
933 forecasting. *Meteorological Applications* **23**(2): 165–181, doi:
934 10.1002/met.1538.
- 935 Cordoba M, Dance S, Kelly G, Nichols N, Waller J. 2017.
936 Diagnosing atmospheric motion vector observation errors for an
937 operational high resolution data assimilation system. *Quarterly
938 Journal of the Royal Meteorological Society* **143**(702): 333–
939 341, doi:10.1002/qj.2925.
- Courtier P, Thepaut J, Hollingsworth A. 1994. A strategy for
operational implementation of 4D-Var, using an incremental
approach. *Quarterly Journal of the Royal Meteorological
Society* **120**(519): 1367–1387, doi:10.1002/qj.49712051912.
- Daley R. 1991. *Atmospheric data analysis*. Cambridge University
Press: Cambridge, UK.
- Davies T, Cullen MJP, Malcolm AJ, Mawson MH, Staniforth
A, White AA, Wood N. 2005. A new dynamical core
for the met office's global and regional modelling of the
atmosphere. *Quarterly Journal of the Royal Meteorological
Society* **131**(608): 1759–1782, doi:10.1256/qj.04.101.
- Davis C, Brown B, Bullock R. 2006. Object-based verification of
precipitation forecasts. part i: Methodology and application to
mesoscale rain areas. *Monthly Weather Review* **134**(7): 1772–
1784, doi:10.1175/MWR3145.1.
- de Haan S, Stoffelen A. 2012. Assimilation of high-resolution
mode-s wind and temperature observations in a regional nwp
model for nowcasting applications. *Weather and Forecasting*
27(4): 918–937, doi:10.1175/WAF-D-11-00088.1.
- Descombes G, Auligné T, Vandenberghe F, Barker DM.
2015. Generalized background error covariance matrix model
(GEN_BE v2.0). *Geosci. Model Dev.* **8**(3): 669–696, doi:10.
5194/gmd-8-669-2015.
- Desroziers G, Berre L, Chapnik B, Poli P. 2005. Diagnosis
of observation, background and analysis-error statistics
in observation space. *Quarterly Journal of the Royal
Meteorological Society* **131**(613): 3385–3396, doi:10.1256/qj.
05.108.
- Dixon M, Li Z, Lean H, Roberts N, Ballard S. 2009. Impact
of data assimilation on forecasting convection over the united
kingdom using a high-resolution version of the met office
unified model. *Monthly Weather Review* **137**(5): 1562–1584,
doi:10.1175/2008MWR2561.1.
- Droegmeier K. 1997. The numerical prediction of thunderstorms:
Challenges, potential benefit, and results from real-time
operational test. *WMO Bulletin* **46**(4): 324–336.
- Ebert EE, Damrath U, Wergen W, Baldwin ME. 2003. The WGNE
assessment of short-term quantitative precipitation forecasts.
Bulletin of the American Meteorological Society **84**: 481492.

- 979 Ebert EE, MacBride JL. 2000. Verification of precipitation in
980 weather systems: Determination of the systematic errors. *J.*
981 *Hydrol.* **239**: 179202.
- 982 Fisher M, Andersson E. 2001. Developments in 4D-Var
983 and Kalman Filtering. Technical report, ECMWF. ECMWF
984 Technical Memorandum 347.
- 985 Fowler AM, Dance SL, Waller JA. 2018. On the interaction of
986 observation and prior error correlations in data assimilation.
987 *Quarterly Journal of the Royal Meteorological Society*
988 **144**(710): 48–62, doi:10.1002/qj.3183.
- 989 Gao J, Stensrud DJ. 2012. Assimilation of reflectivity data in a
990 convective-scale, cycled 3dvar framework with hydrometeor
991 classification. *Journal of the Atmospheric Sciences* **69**(3):
992 1054–1065, doi:10.1175/JAS-D-11-0162.1.
- 993 Gilleland EB, Ahijevych D, Brown BG, B C, E EE. 2009. Inter-
994 comparison of spatial forecast verification methods. *Weather*
995 *Forecast* **24**: 1416–1430, doi:10.1175/2009WAF2222269.1.
- 996 Golub GH, Van Loan CF. 1996. *Matrix computations*. Baltimore:
997 The Johns Hopkins University Press, third edn.
- 998 Healy SB, White AA. 2005. Use of discrete Fourier transforms
999 in the 1D-Var retrieval problem. *Quarterly Journal of the*
1000 *Royal Meteorological Society* **131**(605): 63–72, doi:10.1256/qj.
1001 03.193.
- 1002 Ide k, Courtier P, Ghil M, Lorenc AC. 1997. Unified notation
1003 for data assimilation: Operational, sequential and variational.
1004 *Journal of the Meteorological Society of Japan* **75**(1B): 181–
1005 189, doi:n/a.
- 1006 Janjić T, Bormann N, Bocquet M, Carton JA, Cohn SE, Dance SL,
1007 Losa SN, Nichols NK, Potthast R, Waller JA, Weston P. 2017.
1008 On the representation error in data assimilation. *Quarterly*
1009 *Journal of the Royal Meteorological Society* **n/a**(n/a): n/a – n/a,
1010 doi:10.1002/qj.3130.
- 1011 Johnson A, Wang X. 2013. Object-based evaluation of a storm
1012 scale ensemble during the 2009 noaa hazardous weather testbed
1013 spring experiment. *Mon. Wea. Rev.* **141**(n/a): 1079–1098.
- 1014 Jones CD, Macpherson B. 1997. A latent heat nudging scheme
1015 for the assimilation of precipitation data into an operational
1016 mesoscale model. *Meteorological Applications* **4**(3): 269277.
- Lange H, Janjić T. 2016. Assimilation of Mode-S EHS aircraft
observations in COSMO-KENDA. *Monthly Weather Review*
144(5): 1697–1711, doi:10.1175/MWR-D-15-0112.1, URL
<http://dx.doi.org/10.1175/MWR-D-15-0112.1>.
- Lean H, Clark P, Dixon M, Roberts N, Fitch A, Forbes R,
Halliwell C. 2008. Characteristics of high-resolution versions of
the Met Office Unified Model for forecasting convection over
the United Kingdom. *Monthly Weather Review* **136**(9): 3408–
3424, doi:10.1175/2008MWR2332.1.
- Liu ZQ, Rabier F. 2003. The potential of high-density
observations for numerical weather prediction: A study
with simulated observations. *Quarterly Journal of the Royal*
Meteorological Society **129**(594): 3013–3035, doi:10.1256/qj.
02.170.
- Lorenc AC, Ballard SP, Bell RS, Ingleby NB, Andrews PLF,
Barker DM, Bray JR, Clayton AM, Dalby T, Li D, Payne TJ,
Saunders FW. 2000. The met. office global three-dimensional
variational data assimilation scheme. *Quarterly Journal of the*
Royal Meteorological Society **126**(570): 2991–3012, doi:10.
1002/qj.49712657002.
- Lorenc AC, Jardak M. 2018. A comparison of hybrid variational
data assimilation methods for global nwp. *Quarterly Journal of*
the Royal Meteorological Society **0**: In press, doi:10.1002/qj.
3401.
- Lorenc AC, Rawlins F. 2005. Why does 4D-Var beat 3D-
Var? *Quarterly Journal of the Royal Meteorological Society*
131(613): 3247–3257, doi:10.1256/qj.05.85.
- Mittermaier MP, Roberts N. 2010. Inter-comparison of spatial
forecast verification methods: Identifying skillful spatial scales
using the fractions skill score. *Wea. Forecasting* **25**: 343–354.
- Pacheco PS. 1997. *Parallel programming with mpi*. Morgan
Kaufmann: San Francisco, USA.
- Piccolo C, Cullen M. 2011. Adaptive mesh method in the Met
Office variational data assimilation system. *Quarterly Journal*
of the Royal Meteorological Society **137**(656): 631–640, doi:
10.1002/qj.801.
- Piccolo C, Cullen M. 2012. A new implementation of the adaptive
mesh transform in the Met Office 3D-Var system. *Quarterly*

- 1055 *Journal of the Royal Meteorological Society* **138**(667): 1560–1094
 1056 1570, doi:10.1002/qj.1880.
- 1057 Rainwater S, Bishop CH, Campbell WF. 2015. The benefits
 1058 of correlated observation errors for small scales. *Quarterly*
 1059 *Journal of the Royal Meteorological Society* **141**(693): 3439–1098
 1060 3445, doi:10.1002/qj.2582.
- 1061 Rawlins F, Ballard SP, Bovis KJ, Clayton AM, Li D, Inverarity
 1062 GW, Lorenc AC, Payne TJ. 2007. The Met Office global four-
 1063 dimensional variational data assimilation scheme. *Quarterly*
 1064 *Journal of the Royal Meteorological Society* **133**(623): 347–1103
 1065 362, doi:10.1002/qj.32.
- 1066 Roberts N. 2008. Assessing the spatial and temporal variation in
 1067 the skill of precipitation forecasts from an nwp model. *Meteoro-*
 1068 *logical Applications, Special Issue: Forecast Verification* **15**(1):
 1069 1631697.
- 1070 Roberts N, Lean H. 2008. Scale-selective verification of rainfall
 1071 accumulations from high-resolution forecasts of convective
 1072 events. *Monthly Weather Review* **136**(1): 78–97, doi:10.1175/
 1073 2007MWR2123.1.
- 1074 Rodwell MJ, Palmer TN. 2007. Using numerical weather
 1075 prediction to assess climate models. *Quarterly Journal of the*
 1076 *Royal Meteorological Society* **133**(622): 129–146, doi:10.1002/
 1077 qj.23.
- 1078 Salonen K, Jrvinen H, Eresmaa R, Niemel S. 2007. Bias
 1079 estimation of doppler-radar radial-wind observations. *Quarterly*
 1080 *Journal of the Royal Meteorological Society* **133**(627): 1501–
 1081 1507, doi:10.1002/qj.114.
- 1082 Seaman R. 1977. Absolute and differential accuracy of analyses
 1083 achievable with specified observation network characteristics.
 1084 *Monthly Weather Review* **105**(10): 12111222, doi:10.1175/
 1085 1520-0493(1977)105(1211:AADAOA)2.0.CO;2.
- 1086 Simonin D, Ballard SP, Li Z. 2014. Doppler radar radial
 1087 wind assimilation using an hourly cycling 3d-var with a 1.5
 1088 km resolution version of the met office unified model for
 1089 nowcasting. *Quarterly Journal of the Royal Meteorological*
 1090 *Society* **140**(684): 2298–2314, doi:10.1002/qj.2298.
- 1091 Skok G. 2015. Analysis of fraction skill score properties for a
 1092 displaced rainband in a rectangular domain. *Met. Apps* **22**:
 1093 477484, doi:10.1002/qj.2298.
- Stewart LM. 2010. Correlated observation errors
 in data assimilation. PhD thesis, University of
 Reading. [Http://www.reading.ac.uk/maths-and-](http://www.reading.ac.uk/maths-and-)
 stats/research/theses/maths-phdtheses.aspx.
- Stewart LM, Cameron J, Dance SL, English S,
 Eyre JR, Nichols NK. 2009. Observation error
 correlations in IASI radiance data. Technical report,
 University of Reading. Mathematics reports series,
www.reading.ac.uk/web/FILES/maths/obs_error_IASI_radiance.pdf
- Stewart LM, Dance SL, Nichols NK. 2008. Correlated observation
 errors in data assimilation. *International Journal for Numerical*
Methods in Fluids **56**(8): 1521–1527, doi:10.1002/fld.1636.
- Stewart LM, Dance SL, Nichols NK. 2013. Data assimilation with
 correlated observation errors: experiments with a 1-D shallow
 water model. *Tellus A* **65**(1): 19 546, doi:10.3402/tellusa.v65i0.
 19546.
- Stewart LM, Dance SL, Nichols NK, Eyre JR, Cameron J. 2014.
 Estimating interchannel observation-error correlations for IASI
 radiance data in the Met Office system. *Quarterly Journal of*
the Royal Meteorological Society **140**(681): 1236–1244, doi:
 10.1002/qj.2211.
- Strajnar B, agar N, Berre L. 2015. Impact of new aircraft
 observations mode-s mrrar in a mesoscale nwp model. *Journal*
of Geophysical Research: Atmospheres **120**(9): 3920–3938,
 doi:10.1002/2014JD022654.
- Sun J, Xue M, Wilson JW, Zawadzki I, Ballard SP, Onvlee-
 Hooimeyer J, Joe P, Barker DM, Li PW, Golding B, Xu
 M, Pinto J. 2014. Use of NWP for nowcasting convective
 precipitation: Recent progresses and challenges. *Bulletin of the*
American Meteorological Society **95**(3): 409–426, doi:10.1175/
 BAMS-D-11-00263.1.
- Tabcart J, Dance SL, Haben SA, Lawless AS, Nichols NK,
 Waller JA. 2018. The conditioning of least squares problems
 in variational data assimilation. *Numerical Linear Algebra with*
Applications doi:10.1002/nla.2165.
- Tang Y, Lean HW, Bornemann J. 2013. The benefits of the
 Met Office variable resolution NWP model for forecasting
 convection. *Meteorological Applications* **20**(4): 417–426, doi:
 10.1002/met.1300.

- 1133 Velden C, Lewis WE, Bresky W, Stettner D, Daniels J, Weston PP, Bell W, Eyre JR. 2014. Accounting for correlated error 1172
 1134 Wanzong S. 2017. Assimilation of high-resolution satellite- in the assimilation of high-resolution sounder data. *Quarterly* 1173
 1135 derived atmospheric motion vectors: Impact on hwrf forecasts *Journal of the Royal Meteorological Society* **140**(685): 2420– 1174
 1136 of tropical cyclone track and intensity. *Monthly Weather Review* 2429, doi:10.1002/qj.2306. 1175
 1137 **145**(3): 1107–1125, doi:10.1175/MWR-D-16-0229.1. Wlasak MA, Cullen MJF. 2014. Modelling static 3d spatial 1176
 1138 Waller JA, Ballard SP, Dance SL, Kelly G, Nichols NK, Simonin background error covariances - the effect of vertical and 1177
 1139 D. 2016a. Diagnosing horizontal and inter-channel observation horizontal transform order. *Advances in Science and Research* 1178
 1140 error correlations for SEVIRI observations using observation- **11**(1): 63–67, doi:10.5194/asr-11-63-2014. 1179
 1141 minus-background and observation-minus-analysis statistics. Yaremchuk M, D’Addezio JM, Panteleev G, Jacobs G. 2018. On 1180
 1142 *Remote Sensing* **8**(7): 581, doi:10.3390/rs8070581. the approximation of the inverse error covariances of high- 1181
 1143 Waller JA, Dance SL, Lawless AS, Nichols NK, Eyre JR. 2014. resolution satellite altimetry data. *Quarterly Journal of the* 1182
 1144 Representativity error for temperature and humidity using the *Royal Meteorological Society* : In pressdoi:10.1002/qj.3336. 1183
 1145 Met Office high-resolution model. *Quarterly Journal of the g* 1184
 1146 *Royal Meteorological Society* **140**(681): 1189–1197, doi:10. 1002/qj.2207.
 1147 1148 Waller JA, Dance SL, Nichols NK. 2016b. Theoretical insight into
 1149 diagnosing observation error correlations using observation-
 1150 minus-background and observation-minus-analysis statistics.
 1151 *Quarterly Journal of the Royal Meteorological Society* **142**:
 1152 418–431, doi:10.1002/qj.2661.
 1153 Waller JA, Simonin D, Dance SL, Nichols NK, Ballard SP. 2016c.
 1154 Diagnosing observation error correlations for Doppler radar
 1155 radial winds in the Met Office UKV model using observation-
 1156 minus-background and observation-minus-analysis statistics.
 1157 *Monthly Weather Review* **144**(10): 3533–3551, doi:10.1175/
 1158 MWR-D-15-0340.1.
 1159 Wang Y, Wang X. 2017. Direct assimilation of radar reflectivity
 1160 without tangent linear and adjoint of the nonlinear observation
 1161 operator in the gsi-based envar system: Methodology and
 1162 experiment with the 8 may 2003 oklahoma city tornadic
 1163 supercell. *Monthly Weather Review* **145**(4): 1447–1471, doi:
 1164 10.1175/MWR-D-16-0231.1.
 1165 Wattrelot E, Caumont O, Mahfouf JF. 2014. Operational
 1166 implementation of the 1d+3d-var assimilation method of radar
 1167 reflectivity data in the arome model. *Monthly Weather Review*
 1168 **142**(5): 1852–1873, doi:10.1175/MWR-D-13-00230.1.
 1169 Weston P. 2011. Progress towards the implementation of
 1170 correlated observation errors in 4D-Var. Technical report, Met
 1171 Office, UK. Forecasting Research Technical Report 560.

Table 1. Experiment details

Experiment	Doppler wind observation error matrix	Doppler wind super-observation thinning distance
Control	Diagonal observation error matrix (Operational)	6 km
Corr-R-6km	Correlation observation error matrix	6 km
Corr-R-3km	Correlation observation error matrix	3 km
Diag-R-3km	Diagonal observation error matrix (Operational)	3 km

Table 2. Trial average (μ) and standard deviation (σ) of various parameters measuring the performance of the assimilation system.

Experiments	Iteration count		Evaluation count		J_b		J_o	
	μ	σ	μ	σ	μ	σ	μ	σ
Control	27.4	15.1	40.8	23.5	1752.16	526.1	9207.53	2707.16
Corr-R-6km	27.7	14.6	41.6	22.8	1722.43	500.37	9235.66	2732.84
Corr-R-3km	28.2	14.4	40.9	21.6	2050.53	761.25	10134.63	3175.32
Diag-R-3km	29.1	14.9	41.5	23.8	2277.59	910.74	9679.28	2900.41

Table 3. Computational cost in seconds. The first row shows the trial average wall-clock time ($\overline{W}^{(trial)}$). Subsequent rows show the average wall-clock time ($\overline{W}^{(10)}$), the average cost for calculating J ($\overline{J}^{(10)}$), and the average cost for calculating J_o ($\overline{J}_o^{(10)}$), over 10 iterations for the 12 Z run on the 7th of April 2016.

	Control	Corr-R-6km	Corr-R-3km
$\overline{W}^{(trial)}$ [s]	272	293	288
$\overline{W}^{(10)}$ [s]	73	72	73
$\overline{J}^{(10)}$ [s]	22.16	23.83	23.43
$\overline{J}_o^{(10)}$ [s]	0.81	2.21	2.23

Table 4. Surface verification scores and UK NWP index. All the values are presented as a percentage (positive values show improvement over the Control).

Score	Corr-R-6km	Corr-R-3km
Visibility	+0.027	+0.046
Precipitation	-0.063	-0.050
Cloud cover	+0.047	+0.012
Cloud base height	-0.013	-0.005
1.5m temperature	-0.014	+0.005
10 m wind	+0.010	+0.013
UK index	-0.005	+0.021

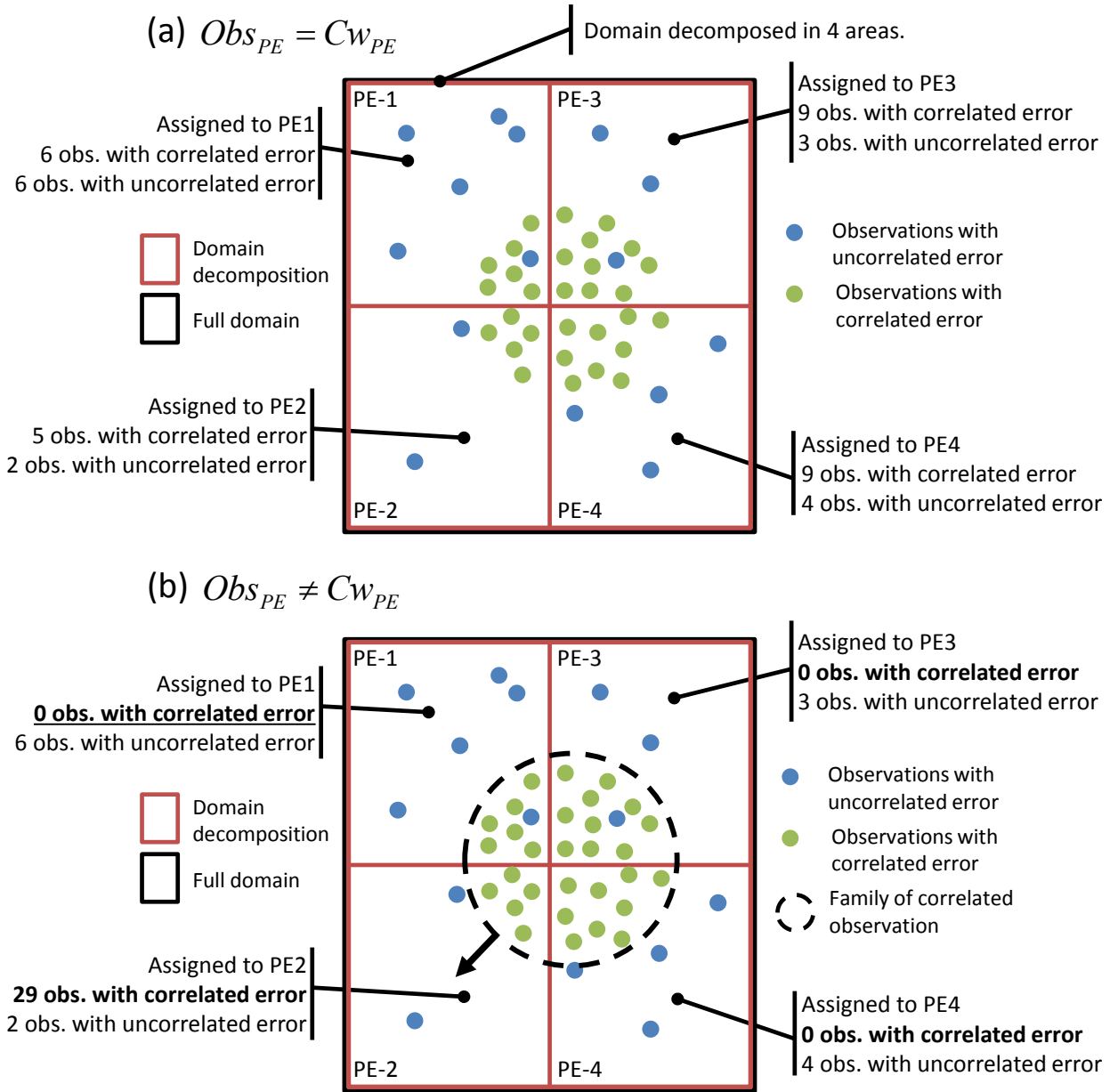


Figure 1. Example of the observation parallelisation in VAR for two observation types (uncorrelated and correlated error) with a 4 PE decomposition. (a) Conventional approach, i.e. without accounting for the horizontal correlation of the observation error. Each observation (with uncorrelated and correlated errors) is distributed between the 4 PE according to its geographical location. (b) The new approach i.e. accounting for the horizontal correlation of the observation error. As before, each observation with uncorrelated error statistics is distributed between the 4 PE according to its geographical location. However, this time all the observations with mutually correlated errors are assigned to a single family and sent to PE 2 regardless of their physical location. In both panels the model columns (C_w) are distributed according to their geographical location. This implies that the distribution of each C_w and observation is equivalent in (a) that is $Obs_{PE} = Cw_{PE}$, and different in (b) i.e. $Obs_{PE} \neq Cw_{PE}$.

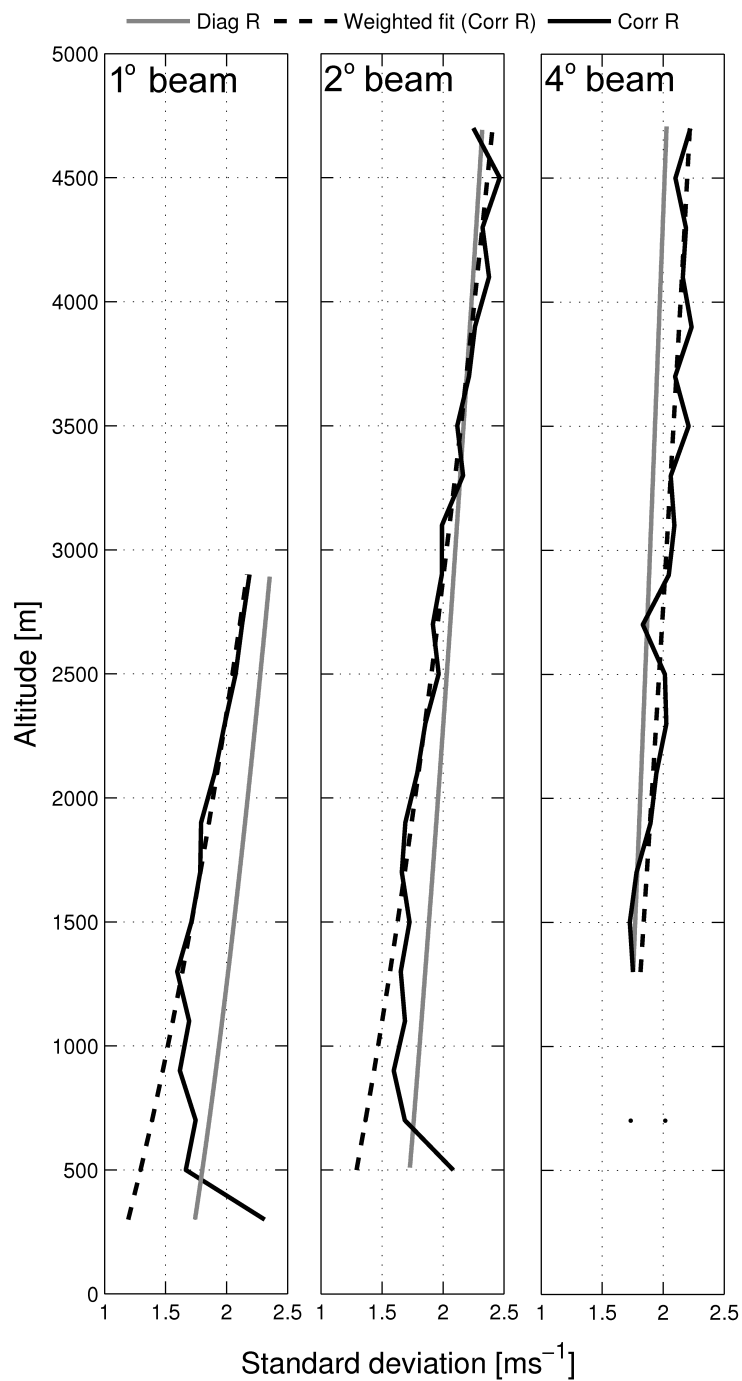


Figure 2. Error variance as function of height for three radar's beam elevation (1° , 2° and 4°). (Grey curve) operational error variance used in the Control experiment when the observation error covariance matrix is assumed to be diagonal. (Black curve) error variance for the diagnosed correlated observation error covariance matrix. (Black dash curve) weighted least square fit of the error variance for the diagnosed correlated observation error covariance matrix used in the Corr-R-6km and Corr-R-3km experiments.

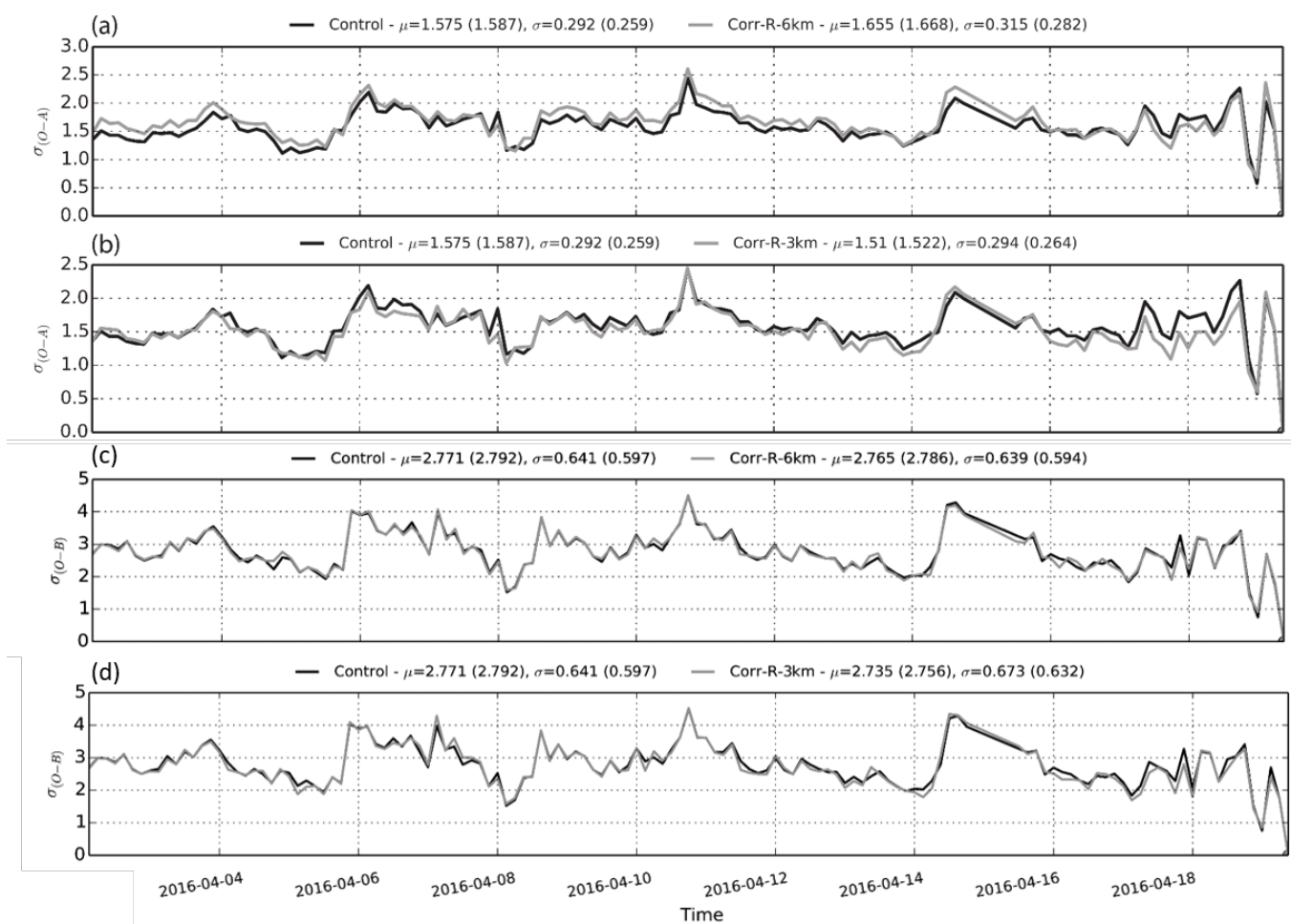


Figure 3. Time series standard deviation of Doppler radial wind $O - A$ (a,b) and $O - B$ (c,d) for the Control and Corr-R-6km (a,c) and for the Control and Corr-R-3km (b,d). In both panels the Control is in black and the experiment in grey.

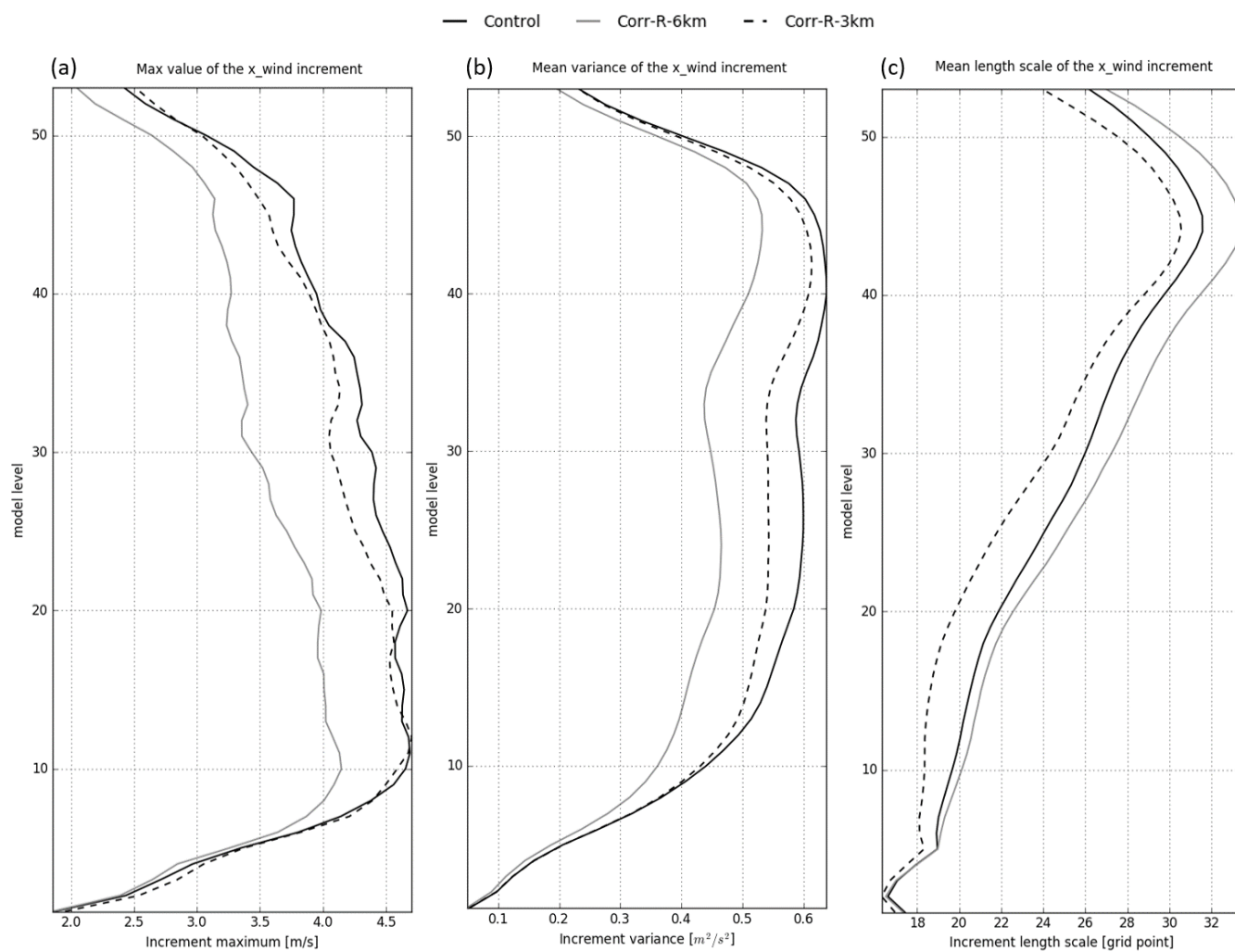


Figure 4. Trial average (a) maximum (b) variance and (c) length-scale (eq 6) for the zonal wind increment against model levels. (Black Curve) Control experiment; (grey curve) Corr-R-6km experiment and (black dash curve) Corr-R-3km experiment.

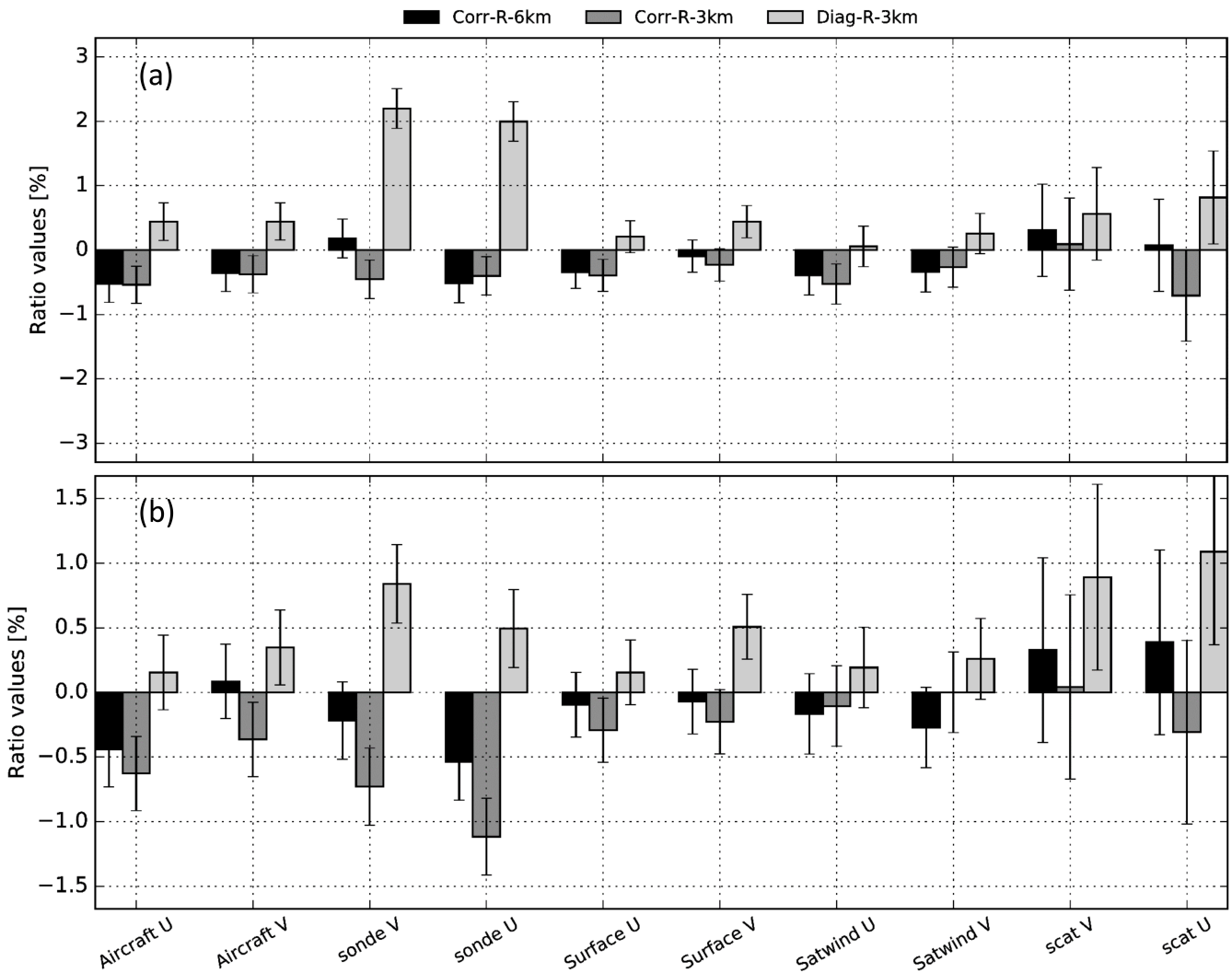


Figure 5. Wind observations (a) $O - A$ and (b) $O - B$ trial average standard deviation ratio between the experiments and the Control expressed as percentage and scaled to show positive impact as negative values (i.e. $\frac{\sigma_{(O-A)_{exp}}}{\sigma_{(O-A)_{ctrl}}} - 1$ and $\frac{\sigma_{(O-B)_{exp}}}{\sigma_{(O-B)_{ctrl}}} - 1$). In black $exp = \text{Corr-R-6km}$, in dark grey $exp = \text{Corr-R-3km}$ and in light grey $exp = \text{Diag-R-3km}$. The error bars represent the 95% confidence level.

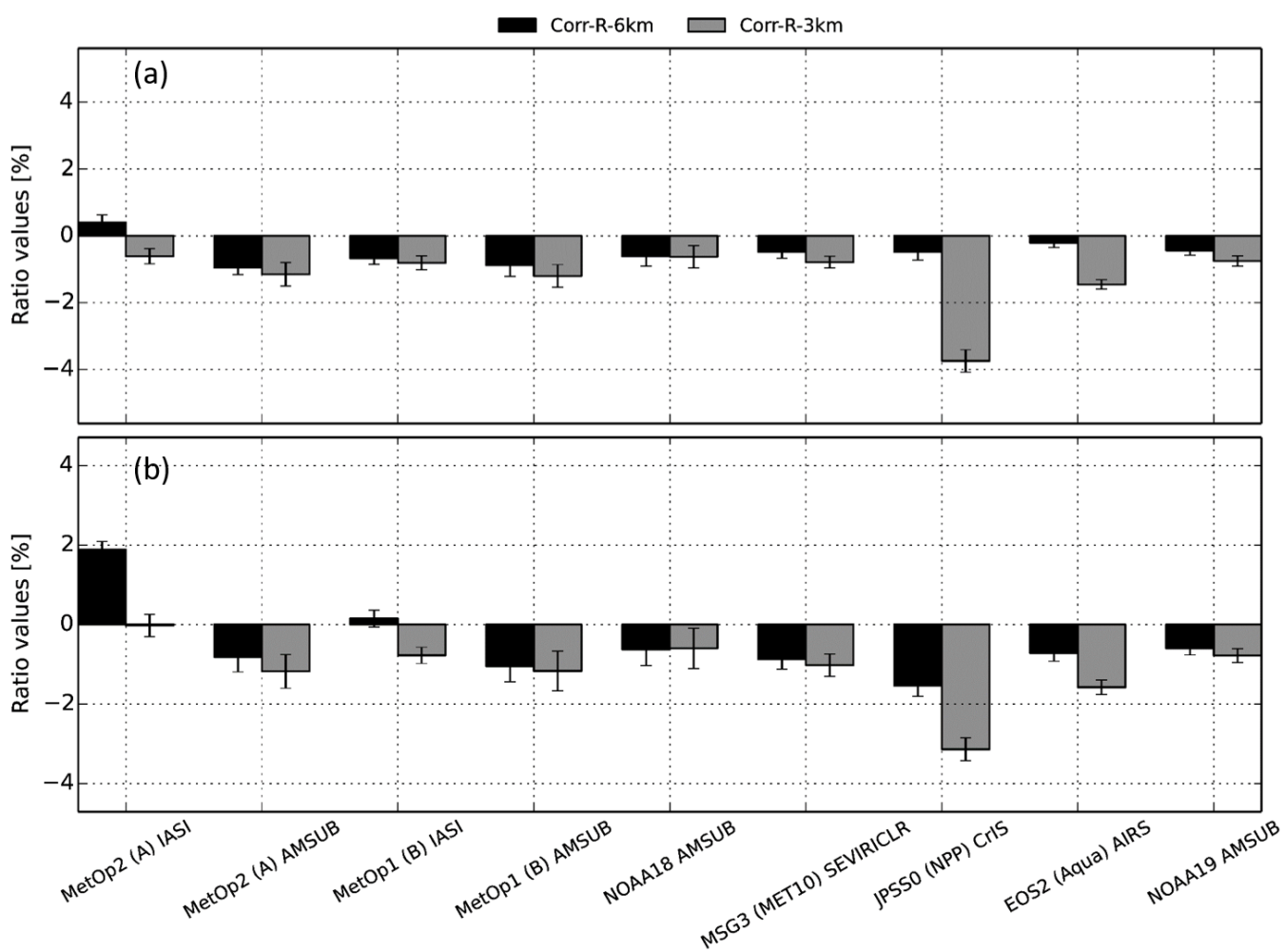


Figure 6. Similar to 5 but for Satellite observations. In black $exp = Corr-R-6km$ and in dark grey $exp = Corr-R-3km$.

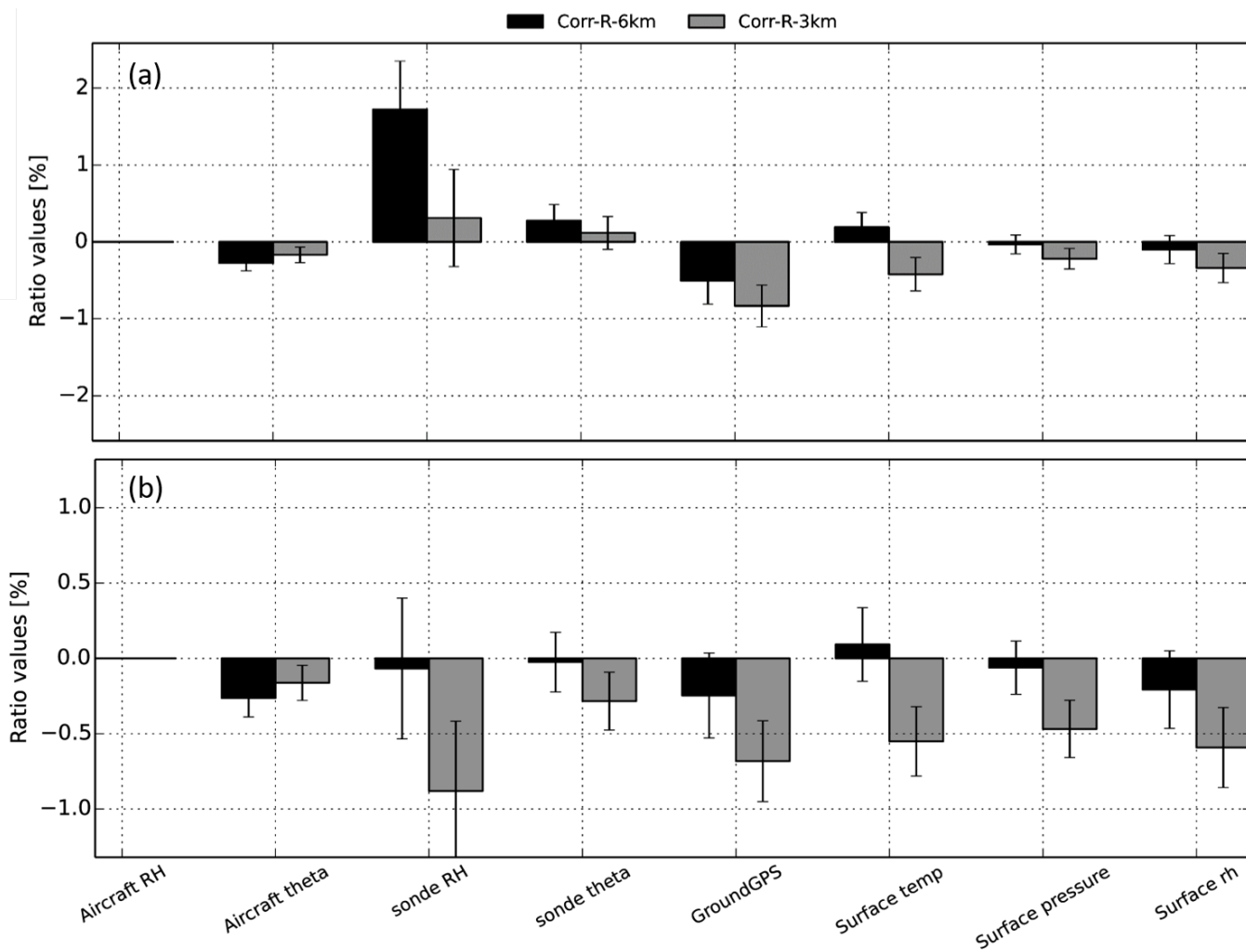


Figure 7. Similar to 6 but for the rest of the observations used.

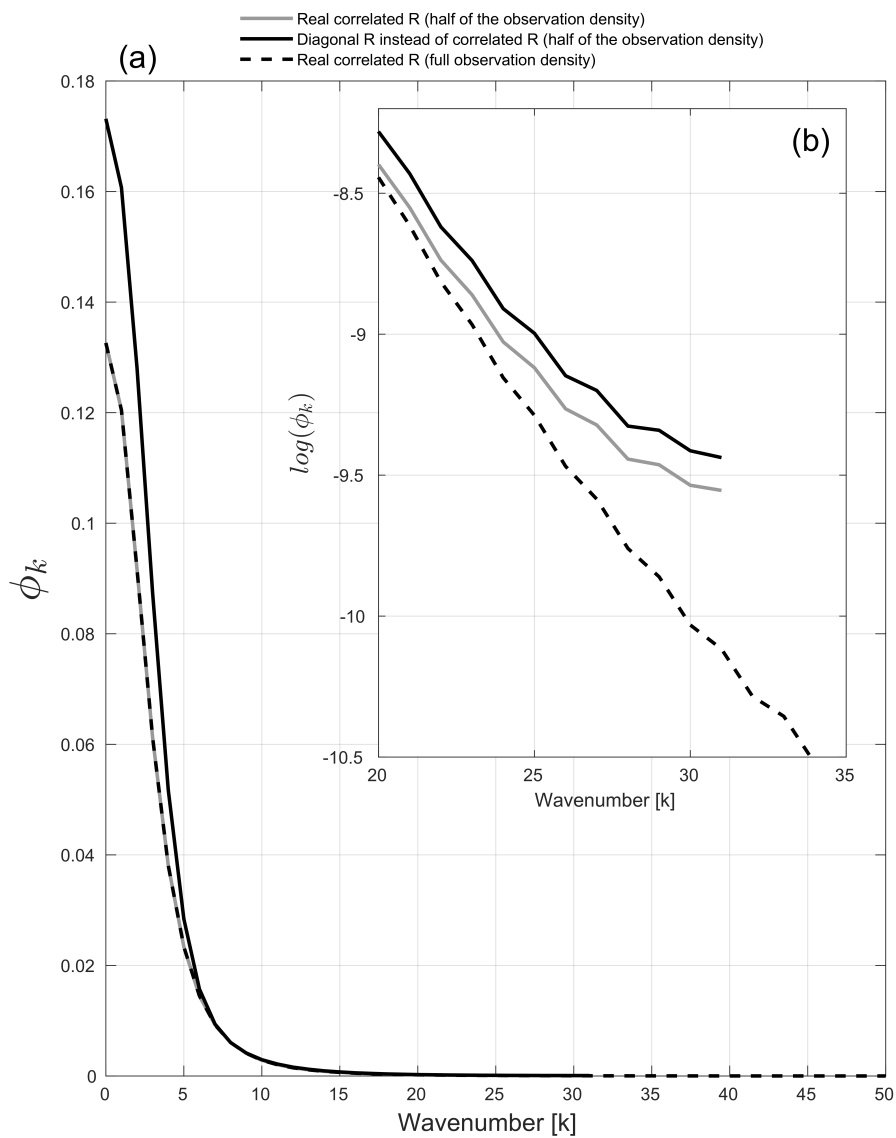


Figure 8. Panel (a) shows the eigenvalues of the analysis error covariance matrix (ϕ_k) in observation space (see appendix for details) against wavenumber. Insert (b) shows ϕ_k in log space for wavenumber ranging from 20 to 35. (Black curve) ϕ_k using a diagonal observation error covariance when the true observation error covariance contains some correlation with the state being half observed. (Grey curve) ϕ_k using a correlated observation error covariance with the state being half observed. (Black dashed curve) ϕ_k using a correlated observation error covariance with the state being fully observed.

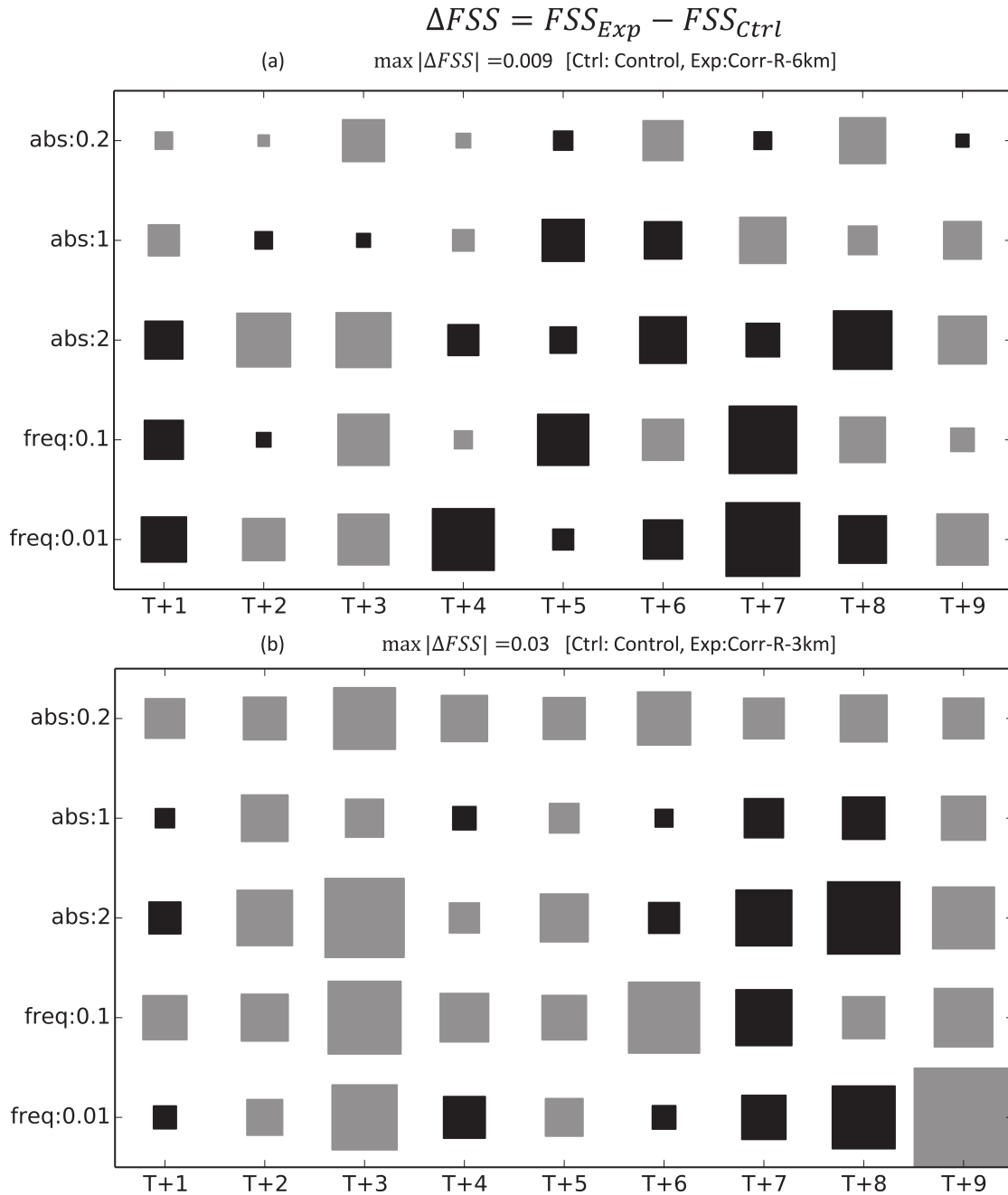


Figure 9. Hinton diagram showing the trial average FSS differences between the Corr-R-6km and the Control experiment (a) and between the Corr-R-3km and the Control experiment (b) for different forecast lead time and hourly rainfall accumulation thresholds with a neighborhood size of 41 grid-boxes. The sign and the amplitude of the change in FSS are shown with the color and size of the square respectively: positive values (positive impact) are shown as gray squares, whereas negative values (negative impact) are shown as black squares. The rainfall accumulation thresholds on y-axis are 0.2mmh^{-1} (abs:0.2), 1.0mmh^{-1} (abs:1), 2.0mmh^{-1} (abs:2), the 90th percentiles (freq:0.1) and the 99th percentiles (freq:0.01).

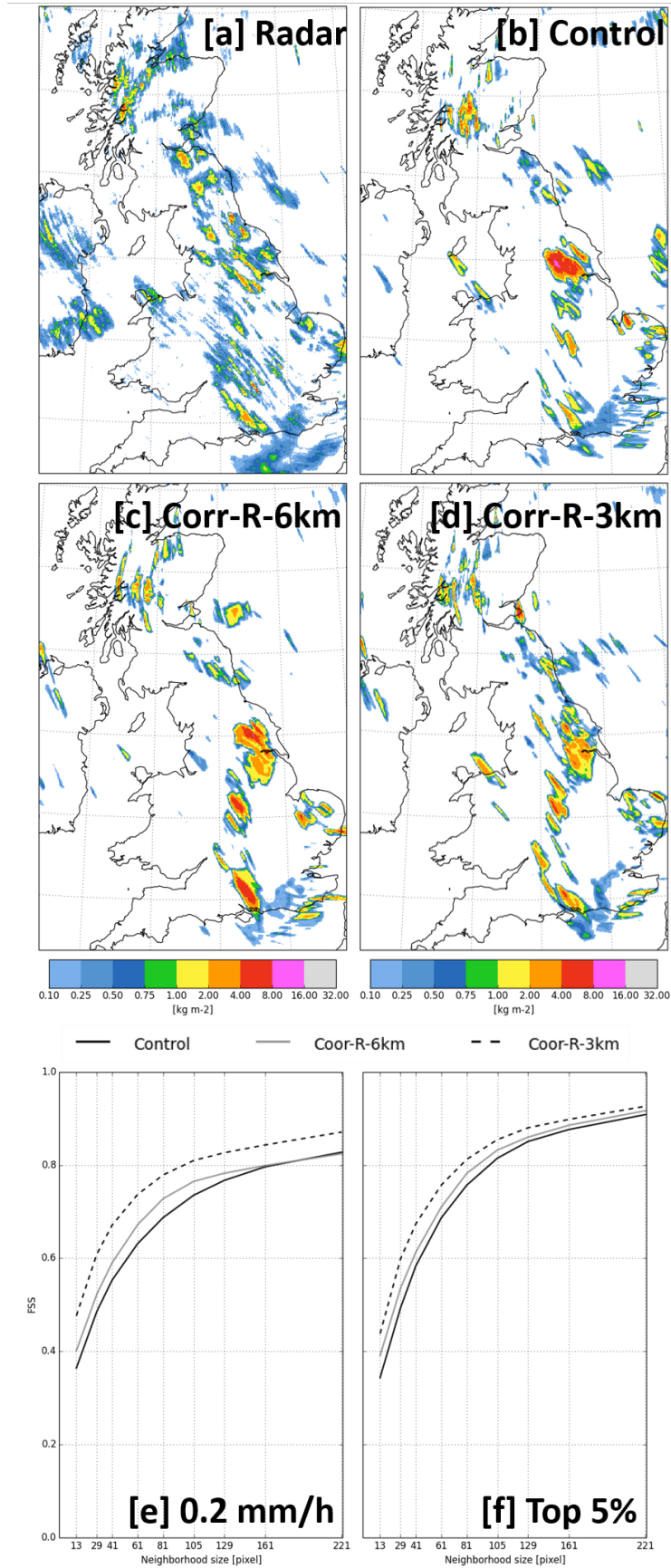


Figure 10. Hourly accumulated precipitation forecasts for 1500 UTC on the 7th of April 2016, for Control [b], Coor-R-6km [c] and Coor-R-3km [d] at T+3. Panel [a] shows the observed radar derived hourly rain accumulation at 1500 UTC. Panels [e] and [f] show the FSS as a function of neighbourhood size for the forecast experiments using thresholds of 0.2mm/h and top 5% (95th percentile) respectively.